Microscopy and Microanalysis, 2023, **00**, 1–19
https://doi.org/10.1093/micmic/ozac032

Original Article

Microscopy AND Microanalysis

Micro- and Nanoscale Surface Analysis of Late Iron Age Glass from Broborg, a Vitrified Swedish Hillfort

Bethany E. Matthews[1,*], James J. Neeway[1], Lorena Nava Farias[1], José Marcial[1], Bruce W. Arey[1], Jennifer Soltis[1], Libor Kovarik[1], Zihua Zhu[1], Michael J. Schweiger[2], Nathan Canfield[1], Tamas Varga[1], Mark E. Bowden[1], Jamie L. Weaver[3], John S. McCloy[4], Rolf Sjöblom[5], Eva Hjärthner-Holdar[6], Mia Englund[6], Erik Ogenhall[6], Edward P. Vicenzi[7], Claire L. Corkhill[8], Clare Thorpe[8], Russell J. Hand[8], David K. Peeler[1], Carolyn I. Pearce[1], and Albert A. Kruger[9]

[1]*Pacific Northwest National Laboratory, Richland, WA 99354, USA*
[2]*DOE Consultant, Richland, WA 99354, USA*
[3]*Material Measurement Laboratory, National Institute of Standards and Technology, Gaithersburg, MD 20899, USA*
[4]*Washington State University, PO Box 642920, Pullman, WA 99164, USA*
[5]*Luleå University of Technology, Luleå SE-971 87, Sweden*
[6]*Geoveta AB, Sjöängsvägen 2, 19272 Sollentuna, Sweden*
[7]*Smithsonian Institution, Museum Conservation Institute, 4610 Silver Hill Road, Suitland, MD 20746, USA*
[8]*Department of Materials Science & Engineering, The University of Sheffield, Sheffield S1 3JD, UK*
[9]*Department of Energy, Office of River Protection, Richland, WA 99352, USA*

***Corresponding author:** Bethany E. Matthews, E-mail: bethany.matthews@pnnl.gov

Abstract

Archaeological glasses with prolonged exposure to biogeochemical processes in the environment can be used to understand glass alteration, which is important for the safe disposal of vitrified nuclear waste. Samples of mafic and felsic glasses with different chemistries, formed from melting amphibolitic and granitoid rocks, were obtained from Broborg, a Swedish Iron Age hillfort. Glasses were excavated from the top of the hillfort wall and from the wall interior. A detailed microscopic, spectroscopic, and diffraction study of surficial textures and chemistries were conducted on these glasses. Felsic glass chemistry was uniform, with a smooth surface showing limited chemical alteration (<150 nm), irrespective of the position in the wall. Mafic glass was heterogeneous, with pyroxene, spinel, feldspar, and quartz crystals in the glassy matrix. Mafic glass surfaces in contact with topsoil were rougher than those within the wall and had carbon-rich material consistent with microbial colonization. Limited evidence for chemical or physical alteration of mafic glass was found; the thin melt film that coated all exposed surfaces remained intact, despite exposure to hydraulically unsaturated conditions, topsoil, and associated microbiome for over 1,500 years. This supports the assumption that aluminosilicate nuclear waste glasses will have a high chemical durability in near-surface disposal facilities.

Key words: alteration, late Iron Age glass, low activity radioactive waste glass

Introduction

Glasses, minerals, and metals will start to alter when exposed to aqueous environments. The rate at which a material alters is largely a function of chemical composition, temperature, solution chemistry, and several other variables (White & Brantley, 2003; Verney-Carron et al., 2008; Pierce et al., 2010; Verney-Carron et al., 2010*a*, 2010*b*; Weaver et al., 2016; Neeway et al., 2018; McCloy et al., 2019). Understanding the effects of these variables on the durability of glass exposed to natural environments may: (i) allow the service lifetime of industrial materials to be extended; (ii) provide better methods for conserving cultural heritage materials; and (iii) increase public acceptance of vitrified nuclear waste disposal. Here, anthropogenic glass present in the vitrified wall (a structure or wall cemented together by a melting of rock into glass) of the ≈1500-year-old Broborg hillfort (a defensible place surrounded by, in this case, a ridge or wall) in Sweden is presented as an example of a glass that can be used to better understand the behavior of glass that has been exposed to the natural environment (Sjöblom et al., 2016; Weaver et al., 2016; Weaver et al., 2018). Beyond knowledge of the age of the vitrified hillfort, the temperature, rainfall, and groundwater chemistry at the site for the lifetime of the hillfort are relatively well understood. A primary focus of studying the archaeological remains at Broborg is to provide a basis for understanding key processes that occur at the interface between glasses of different chemistries and the natural environment, by examining the thickness, morphology, and compositional variation of the surficial layer on the analog glass in a relatively well-understood environment (Macquet & Thomassin, 1992).

The Broborg hillfort has been the subject of several studies. The hillfort was likely abandoned a few hundred years after it had been constructed and has remained relatively undisturbed (Sjöblom et al., 2022). The local soil chemistry was influenced by the heating of the surrounding gneissic granite during the vitrification. A recent excavation measured topsoil average

Received: August 17, 2021. **Revised:** May 29, 2022. **Accepted:** September 15, 2022

pH to be 6.5, which was over a unit less than the value (pH 8) measured for the red gravel fines overlaying the vitrified region of the wall. The hillfort and surrounding area have been exposed to acid rain towards the end of the 20th century. The present annual precipitation at Broborg is 572 mm and the average annual temperature is 5°C. There have been some climate changes, i.e., certain variations in rainfall and temperature (Nava-Farias et al., 2021; Plymale et al., 2021; Sjöblom et al., 2022). Thus, Broborg hillfort glasses offer the potential to study glass alteration behavior in a near-surface environment, under the generally temperate conditions at Broborg.

Knowledge of the environment is especially relevant to nuclear waste glass isolation where disposal environments will be selected that will minimize, to the best extent possible, the degradation of the nuclear waste glass and thus limit the release of radionuclides into the near-field environment.

The issue of nuclear waste glass disposal is relevant in many countries that have selected vitrification as the preferred method of waste immobilization (Vernaz & Bruezière, 2014). To supplement this research, analog archeological glass samples that have altered in natural environments for even longer time periods, but considerably lower temperatures, have been used to gain insight into the probability of the alteration mechanisms proposed in glass alteration models (Ewing & Roed, 1987; Crovisier et al., 1988; Macquet & Thomassin, 1992; Murphy, 2000; Rani et al., 2010; Verney-Carron et al., 2010*a*, 2010*b*; Michelin et al., 2013; Sjöblom et al., 2013; Sjöblom et al., 2016; Weaver et al., 2018), specifically in regards to thermodynamic and kinetic assumptions that have been developed from short-term laboratory experiments (Miller et al. 1994).

At present, the largest waste vitrification project in the world is the Waste Treatment and Immobilization Plant (WTP) at the U.S. Department of Energy (DOE) Hanford Site, in Washington State (USA), where 56 million gallons (2.1×10^8 L) of liquid radioactive and chemical waste will be immobilized in glass (Goel et al., 2019). The high-level waste glass is to be disposed of in a geologic repository, and the low-activity waste (LAW) glass will be disposed in the near-surface Integrated Disposal Facility (IDF) at the Hanford Site (DOE, 2017).

Before the LAW glass can be disposed at the Hanford Site IDF, it must be demonstrated that the disposal can be done safely, namely, that radionuclide release will meet regulatory limits (DOE, 2017). Contact between the LAW glass and groundwater is the most effective pathway by which radionuclides can be released from the glass into the environment (Birkholzer et al., 2012). For this reason, models have been developed that capture important processes in complex glass-water interactions and estimate the extent of glass alteration over hundreds to thousands of years (McGrail et al., 2001; Grambow, 2006; Frugier et al., 2008; Verney-Carron et al., 2010*a*, 2010*b*; Vienna et al., 2013; Neeway et al., 2016; Frugier et al., 2018; Rieke et al., 2018). These long-term models are constructed with consideration of predominant glass alteration mechanisms that are observed from controlled laboratory experiments performed over days to several years, and often at temperatures near 90°C, so additional understanding of glass alteration at lower temperatures and longer duration, such as Broborg hillfort samples, are useful. The Broborg hillfort site serves as an environmental analog for the IDF because the glass has been altered near to the Earth's surface in both cases. The 30-year average annual precipitation at the Hanford site is 180 mm (Hoitink et al., 2005), and the average annual temperature at the depth of the IDF is 15–17°C (Freedman et al., 2015), compared to an average annual precipitation of 572 mm and an average annual temperature of 5°C at Broborg. Given the role water plays in accelerating alteration, Broborg should represent a conservative estimate of the expected alteration of LAW glass disposed in the semi-arid environment of the Hanford site IDF (Sjöblom et al., 2013).

Based on its size and strategic position overlooking a waterway, the vitrified hillfort at Broborg is a structure built for control and defense, where the ramparts have been fortified, *in situ* with a vitreous material produced from melting local amphibolite and granitic gneiss lithologies at temperatures on the order of 1200°C (Kresten et al., 1993; Weaver et al., 2016; Weaver et al., 2018; Sjöblom et al., 2022). The vitrified material found at Broborg spans a range of silicate compositions but falls into two distinct categories: a mafic (basalt-like) glass and a felsic glass of "trachyte" composition based on the total-alkali-silica (TAS) diagram (Le Bas et al., 1986; Figure 9 in McCloy et al., 2021). As the amphibolite melted, it formed the less viscous dark glass that flowed over all surfaces, penetrating the space between the gneissic boulders, and serving as a flux to initiate the melting of the gneiss, thus reinforcing the wall structure (Kresten & Ambrosiani, 1992). The felsic melt was estimated to have been nearly two orders of magnitude more viscous than the mafic melt and was formed from inhomogeneous melting of the granitic gneiss (McCloy et al., 2021; Vicenzi et al., 2022). Further description of the melting of different lithologies to form the vitrified hillfort is provided elsewhere (McCloy et al., 2021).

The Broborg aluminosilicate glasses contain several of the same major elements present in LAW aluminosilicate glasses, including sodium (Na), potassium (K), silicon (Si), aluminum (Al), iron (Fe), or elements that perform similar structural roles within the silica glass polymeric framework, but they are not compositionally identical. For example, the Broborg glasses are richer in Si and Al, poorer in Na and Fe, and do not contain boron (B), which is a significant component of LAW glass, with a general target B_2O_3 mass fraction of 0.04–0.16 (Ewing & Roed, 1987; Weaver et al., 2018). However, in neutral to alkaline conditions similar to Broborg, B is not retained in the alteration layer and is not incorporated into secondary phases that form at the glass surface (Scheetz et al., 1985). So, a technical basis may be made that the Broborg aluminosilicate glasses are good analogs for identifying surficial features formed under environmentally relevant conditions (Alexander et al., 2015). The bulk compositions of mafic and felsic glass samples obtained from previous Broborg excavations have been confirmed by several techniques and are shown, along with a typical LAW glass composition, in Table 1 (Kresten & Ambrosiani, 1992; Weaver et al., 2018; Vicenzi et al., 2022).

A previous scanning transmission electron microscopy (STEM) combined with energy dispersive spectroscopy (EDS) study of vitrified material excavated from Broborg in the 1980s showed evidence for the association of a microbial community with the surface of the glass, and revealed potential morphological and chemical alteration (Weaver et al., 2018). Here, microscopic and spectroscopic characterization of Broborg glasses has been conducted to determine the thickness, morphology, and compositional variation of the surficial layer on mafic, lower silica-containing glass and

Table 1. Measured Composition in wt% of Felsic Glass and Mafic Glass from Broborg, Along with a Representative LAW Glass (LAWA44).

	Felsic Glass Composition			Mafic Glass Composition			LAW Glass
Component	μXRF[d]	EPMA[e]	SEM-EDS and μXRF[f]	μXRF[d]	EPMA[e]	SEM-EDS and μXRF[f]	LAWA44[g]
SiO_2	67.4	61.7	63.3	49.0	51.1	55.9	44.5
Al_2O_3	15.1	22.1	20.4	14.2	16.5	13.8	6.2
Na_2O	4.7	5.8	5.	4.8	2.8	3.6	20.0
Fe_2O_3	0.91	1.11	0.3	11.8	10.4	11.0	7.0
CaO	0.2	1.40	1.1	11.3	9.8	6.1	2.0
K_2O	8.9	5.9	7.3	2.4	1.3	2.1	0.5
MgO	1.2	0.26	0.2	2.7	6.2	3.3	2.0
MnO	0.02	0.00	0.04	0.3	0.3	0.3	0.0
P_2O_5	1.4	0.24	0.1	2.0	0.3	0.8	0.0
TiO_2	0.2	0.12	0.1	1.6	0.9	2.0	2.0
Others[a]	–	1.37	0.4	–	0.5	0.3	15.8[c]
Total[b]	**100.0**	**100.0**	**98.5**	**100.0**	**100.0**	**99.8**	**100.0**

The relative uncertainty for the major oxides (defined as ≥ 5 wt%) is $\pm 10\%$ of the oxide.
[a]Others include BaO, B_2O_3, Cl, Cr_2O_3, Cs_2O, CoO, CuO, F, La_2O_3, PbO, Li_2O, MoO_3, NiO, Re_2O_7, SrO, SO_3, SnO_2, WO_3, V_2O_5, ZnO, and ZrO_2.
[b]Values do not sum to 100.0 due to analytical uncertainties and the presence of unanalyzed elements (e.g., H and associated bound oxygen).
[c]In LAWA44, $B_2O_3 = 8.9$ wt%, ZnO = 3.0 wt% and $ZrO_2 = 3.0$ wt%, with remaining other components < 1 wt%.
[d]Adapted from Weaver et al. (2018).
[e]Adapted from Kresten & Ambrosiani (1992).
[f]Adapted from Vicenzi et al. (2022).
[g]Adapted from Pierce et al. (2004).

felsic, high silica-containing glass, after exposure to different environmental conditions. These samples were excavated in 2017 and their location at the site and subsequent storage conditions have been documented (Nava-Farias et al., 2021; Plymale et al., 2021). Cataloging the various surficial features that are formed under near-surface conditions in the environment over hundreds of years contributes to the understanding of the long-term behavior of glass in the environment and provides information on how glass chemistry influences environmental response.

Materials and Methods

Materials

An archaeological excavation of the Broborg hillfort in Uppland was carried out during the summer and fall of 2017 with permission from Uppsala County Administrative Board and funding from the U.S. Department of Energy (DOE) Office of River Protection (Weaver et al., 2018). The survey was a collaboration between The Archaeologists, The National Historical Museums Uppsala, and scientists at: the U.S. DOE Office of River Protection, Pacific Northwest National Laboratory (PNNL), Washington State University (WSU), and Luleå University of Technology. The objectives of this field survey were to: (i) obtain samples of vitrified material for analysis to determine how the near-field environment influenced long-term glass durability and (ii) provide further insight into the anthropological and archeological interpretation of the Broborg site (Englund et al., 2018; Sjöblom et al., 2022).

Bulk sample analysis of the granitic and amphibolitic rocks that represent the starting materials for the glass is given in Ogenhall et al. (2016). Samples of the two glass compositions, mafic and felsic glasses (Table 1), were obtained from the surface of the hillfort wall in contact with topsoil as well as from a wall interior where the samples were partly protected from the environment, for instance from extended exposure to water or from microbial community inhabiting the topsoil. Figure 1a shows the excavation site and the location of the samples. In Figure 1b, a cross-section of the hillfort wall shows the wall surface and the inner wall interior.

The samples extracted for analysis in this study were relatively homogeneous regions of (i) mafic glass from the inner wall (Sample 39, Fig. 1c, red rectangle); (ii) felsic glass from the inner wall (Sample 40, Fig. 1d, blue rectangle); and (iii) felsic glass in contact with topsoil (Sample 11, Fig. 1e, blue circle). A large, heterogeneous, partially vitrified sample (Sample 49), spanning both the outer and inner wall, was also excavated (Fig. 1a, red circle and Supplementary Figs. 1a and 1b). The top of the sample was exposed to the environment and the bottom of the sample was in a wall interior (Supplementary Fig. 1c). The top of Sample 49 was subsectioned to generate a smaller uniform sample of mafic glass in contact with topsoil (Sample 49b, Fig. 1f, red circle and Supplementary Fig. 1d). The five samples characterized in this study are described in Table 2.

Methods

The protocol for sample analysis was outlined in Weaver et al. (2018). The internal microstructure of the samples prior to sectioning was analyzed by XCT. The samples were scanned with a Nikon XTH 320/225 kV high-resolution microfocus tomography scanner (Nikon Metrology, Brighton, MI, USA) using an X-ray energy of 95 kV and 165 μA of source current for optimum image quality and contrast. The samples were rotated during the scans with momentary pauses to collect each projection (shuttling mode) to minimize ring artifacts. For each sample, a total of 3,142 projections were collected over 360° with 708 ms exposure time and four frames per projection. Image pixel resolution was 3.36 μm (voxel size of 38 μm^3). The images were reconstructed to obtain a three-dimensional dataset with CT Pro 3D (Metris XT 2.2, Nikon Metrology).

To gain a better understanding of the relative altering effects of the two environments on the different glass compositions (Table 1), the samples described in Figure 1 and Supplementary Figure 1 and Table 2 were examined by electron microscopy. Subsamples of Sample 49 (Supplementary

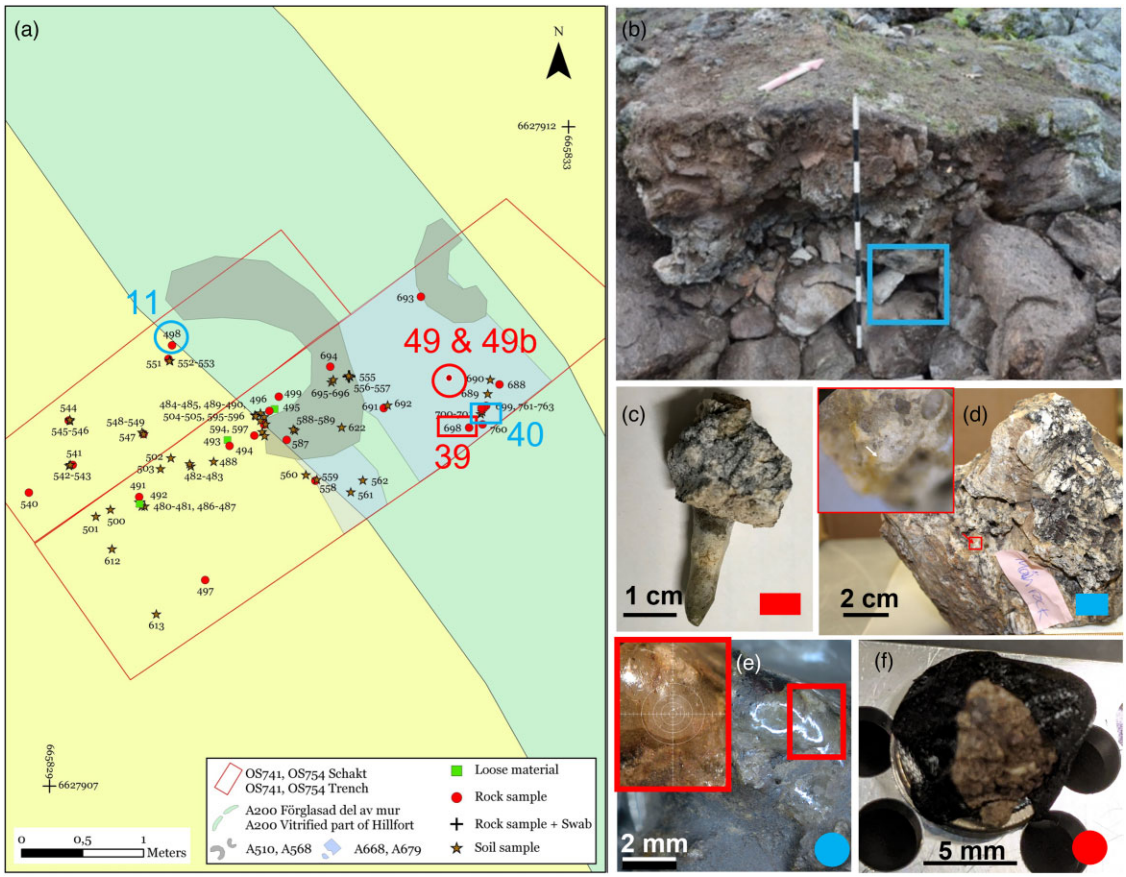

Fig. 1. (**a**) Excavation site map adapted with permission from Englund et al. (2018) showing the sampling locations within the excavation trench (large red rectangles) with samples from the inner wall (smaller bolded blue and red rectangles) and from the topsoil (small bolded blue and red circles) for both felsic glass (blue, left circle and right rectangle) and mafic glass (red, right circle and left rectangle). The numbers in the upper right and bottom left are the coordinates of the survey area (coordination system: $Sweref_{99}$ TM, the Swedish national coordinate system). (**b**) A cross-section of the wall, with meter rule for scale, showing the wall surface and interior (blue box shows a void in the wall interior from which samples were collected). Photographs of (**c**) the mafic glass from wall interior, (**d**) felsic glass from wall interior, (**e**) felsic glass in contact with topsoil, and (**f**) mafic glass in contact with topsoil.

Fig. 1c) from the region in contact with topsoil and from the side with the wall interior were cut and prepared for SEM by first mounting in epoxy and then polishing with diamond paste and nonaqueous lubricants, including colloidal silica. Polishing was performed on a lapidary wheel until the surface roughness was ≈1–10 μm, then on a vibratory polisher to give a final submicron surface finish (surface roughness ≈0.02–0.05 μm) suitable for imaging. The Sample 49 cross-sections from both the topsoil and wall interior were imaged with a JEOL 7001F SEM to examine the altered glass layer on the scale of tens to hundreds of micrometers. The chemistry of the alteration layer at the surface was examined using a 10 kV SEM beam and a Bruker Xflash 6 60 X-ray detector with a spectral resolution of 129 eV. X-ray spectra were processed using Bruker Espirit v2.1 software. Electron backscatter diffraction (EBSD) patterns were generated by a 30 kV electron beam with 29 nA of beam current and were collected and processed using a Bruker Quantax EBSD e-Flash HD detector and Esprit v2.1 software. Simultaneous EBSD and EDS were collected. As there is some latent shift between the initial image collection and the map collect, the EDS and EBSD map images were manually adjusted after collection to account for this drift.

Table 2. Identification and Description of Samples Examined in this Study (Mafic Glass Samples Are Shaded).

Soil Contact Samples	Wall Interior Samples
Mafic glass in contact with topsoil (Sample 49B)	Mafic glass from melted wall interior (Sample 39)
Felsic glass in contact with topsoil (Sample 11)	Felsic glass from melted wall interior (Sample 40)
Top surface of mafic glass from melted wall in contact with topsoil (Sample 49)	Bottom surface of mafic glass from melted wall in wall interior (Sample 49)

Subsamples of mafic glass in contact with topsoil (Sample 49, Supplementary Fig. 1) and of felsic glass in contact with topsoil (Sample 11, Fig. 1e) were analyzed with a Rigaku D/Max Rapid II μ-XRD instrument with an image plate detector. X-rays were produced with a MicroMax 007HF generator fitted with a rotating Cr anode ($\lambda = 0.22897$ nm) and focused on the specimen through a 300 μm diameter collimator. The 2DP, Rigaku 2D Data Processing Software (Ver. 1.0, Rigaku, 2007) was used to integrate the diffraction rings captured by the detector. The analysis of diffraction data was carried out with JADE 8.5 from Materials Data Inc., and the PDF4+database from the Inorganic Crystal Structure Database (ICSD).

To measure the relative thickness of the surficial layer in the two environments, five locations on each of the samples were examined by SEM at a field of view of 2400 μm or 240 μm.

Specific locations were chosen that were representative of the mafic glass and were examined for the depth of the surficial layer. For each SEM scan examined, surficial features with the minimum and maximum thickness were measured and recorded. The thickness of the surficial layer at three additional random areas was measured and recorded, then all five measurements were averaged together to obtain the mean average.

To determine hydration in the surficial layers of cross-sectioned mafic glass examined by SEM, ToF-SIMS measurements were performed at Environmental Molecular Sciences Laboratory (EMSL), located at Pacific Northwest National Laboratory. A TOF.SIMS5 instrument (IONTOF GmbH, Münster, Germany) was used with a 25.0 keV Bi+beam as the analysis beam to collect secondary ion images. To remove surface contamination and control H background (Zhu et al., 2012; Zhang et al., 2019), a 2.0 keV Cs + (about 125 nA, for negative ion imaging) or a 2.0 keV O_2+ (about 350 nA, for positive ion imaging) sputter beam was used before and during analysis. Before data collection, the Cs + or O_2+ beam was scanned over a $700 \times 700\ \mu m^2$ area for 300 s to remove surface contaminations. During imaging data collection, an interlaced mode was used, in which the Bi + beam was used for image data collection, and the Cs + or O_2+ beam was used for H background control. The Bi + beam was focused to a 400 nm diameter with a beam current of about 1.70 pA at 20 kHz frequency. The Bi+beam was scanned over a $500 \times 500\ \mu m^2$ (or $200 \times 200\ \mu m^2$) area with 256×256 pixels. The Cs+ or O_2+ beam was scanned over a $700 \times 700\ \mu m^2$ area, and the Bi+beam was prealigned to the center of the Cs+ or O_2+ sputter crater. For brevity, only the positive ion results are shown.

The small, relatively homogeneous samples (Figs. 1c–1f) were prepared for SEM analysis by sectioning appropriately sized pieces (<5 cm in any dimension) and then coating with 20 nm of carbon to reduce, although not completely eliminate, electron beam charging. Samples were examined using an FEI Dual-beam Helios Nanolab 660 FIB-SEM to analyze the micron and nanometer scale features on the surface morphology of the glass. Imaging was performed primarily at 3 and 5 kV using beam currents of 0.1–3.2 nA and a working distance of 4 mm. An Everhart-Thornley secondary electron (SE) detector was used in the field-free mode for SE imaging, and a through-the-lens detector was used for SE and backscatter electron imaging in immersion mode.

Regions from the exposed glass surface as well as cracks in the glass were prepared as cross-sectional samples for STEM with the FEI Dual-beam Helios Nanolab 660 FIB-SEM. Extracted lamellae for STEM analysis typically extend to 10–15 μm below the surface. Accordingly, all sites selected for FIB-STEM lift-out and examination were taken from relatively flat regions of the specimens. These lift-out regions were first coated by a 300 nm layer of platinum (Pt) using the electron beam and then 3 μm of C using the gallium (Ga) ion beam to protect the uppermost surface during ion milling. The thin foils were then removed from the surface by a standard lift-out procedure using a 30 keV Ga ion beam, attached with Pt to a copper (Cu) transmission electron microscopy (TEM) half-grid, and thinned to electron transparency using progressively lower ion beam energies ending with final thinning at 5 keV and a final polish at 2 keV. The selected regions were examined by an aberration-corrected JEOL-ARM 200CF microscope operating at an accelerating voltage of 200 kV with a convergence semi-angle of 27.5 mrad and an inner collection angle of 68 mrad. STEM-EDS mapping was also performed using a JEOL Centurio EDS detector setup, with a 0.1–1 nm probe size, 0.12–1 nA probe current, and 5–15 min total acquisition time. The cross-sections were imaged by TEM prior to STEM-EDS, since STEM-EDS resulted in beam damage to these beam-sensitive samples. TEM analysis was performed using the FEI Titan 80–300 operated at 300 kV. The microscope is equipped with CEOS aberration corrector for the probe-forming lens, which enables subangstrom image resolution in STEM mode. Selected area electron diffraction (SAED) was collected in high-resolution TEM (HRTEM) mode. Simulations of electron diffraction patterns for comparison were conducted using SingleCrystal by CrystalMaker Software. Compositional analysis was performed with an EDX Si(Li) EDS detector. When performing EDS mapping analysis, the electron dose rate impinging on the sample was minimized by subpixel scanning, and artificially defocusing the probe to reduce electron density until no significant damage was observed on the sample.

Results and Discussion

Surficial Examination of Felsic and Mafic Glass Samples

To compare the extent of alteration that occurred on glasses from the melted wall interior and from the top surface of the wall in contact with topsoil, felsic and mafic glass samples from both regions were examined. μ-XRD analysis of the felsic glass (Supplementary Fig. 2) confirmed it to be amorphous, with a large background and only one broad peak that corresponds to the most intense quartz peak (101). μ-XRD analysis of mafic glass (Supplementary Fig. 3) confirmed that it had a significant amorphous component with an elevated background and broad diffraction peaks. The crystalline phases present in the mafic glass were identified as spinel, quartz, feldspar, and pyroxene.

Felsic Glass from the Melted Wall Interior

Felsic glass from the wall interior (Sample 40) is visible as a sheen on the surface of the sample and occasionally contains bubbles or vesicles (Fig. 1d). The vesicles in the material are fragile and several broken bubble-like features are present near the surface. These vesicles, or voids, were formed as a result of volatiles released during the melting (McCloy et al., 2021). Figure 2 shows that the felsic glass is smooth and surrounded by rougher regions. SEM-EDS (Fig. 2c) of the bubble of felsic glass shows the smooth regions are richer in Si, Al, and Na, consistent with the composition of felsic glass (Table 1). Quantification of the EDS maps comparing the smooth, Si-rich regions to the rough, C-rich regions is shown in the table in Figure 2. The largest difference between the two regions apart from the substantial increase in C is a reduction of Si, Al, and K and an increase in Ca, Mg, Ti, and Fe, as detailed in the table in Figure 2.

Cross-sections were extracted by FIB for STEM analysis, exposing the interior void of a felsic glass bubble (Fig. 2a). STEM imaging and EDS (Fig. 3) showed that the cross-section was relatively uniform but contained inclusions EDS of the inclusions showed they had two compositions, one containing C, K, N, and O and the other containing S, K, and O (EDS spectrum shown in Supplementary Fig. 4a). Attempts to characterize the phase of the particles by selected area diffraction (SAED), showed the general matrix of the glass was amorphous, in

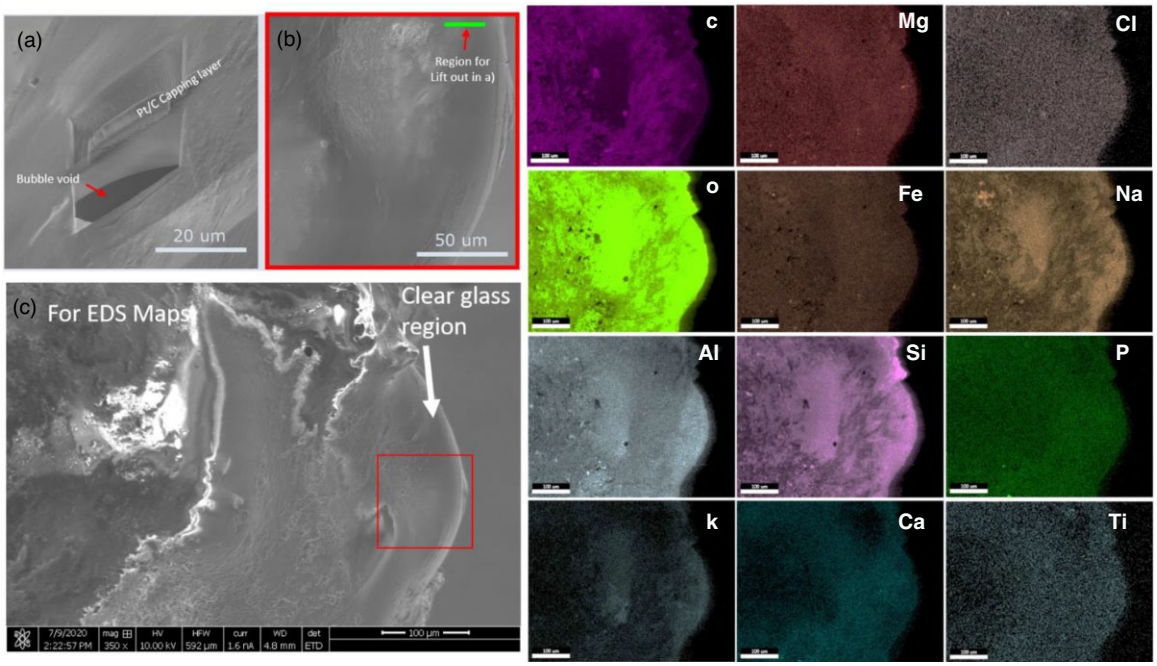

Oxide	Wt%	
	Si-rich region	C-rich region
Fe_2O_3	2.74%	22.69%
Na_2O	5.66%	6.53%
MgO	0.53%	3.99%
Al_2O_3	15.67%	15.31%
SiO_2	64.73%	38.60%
K_2O	7.15%	3.39%
CaO	2.87%	6.53%
TiO_2	0.66%	2.96%
Total	100%	100%

Fig. 2. SEM images (**a–c**) felsic glass (Sample 40) from the wall interior. FIB milling in (**a**) expose the void inside a glass bubble. A higher resolution image of the square in (**c**) is shown in (**b**). Net counts EDS maps (scale bar = 100 μm) corresponding to (**c**) are shown. Table (bottom) shows the wt% of oxides for the Si-rich region and the C-rich region with relative uncertainty ±10%.

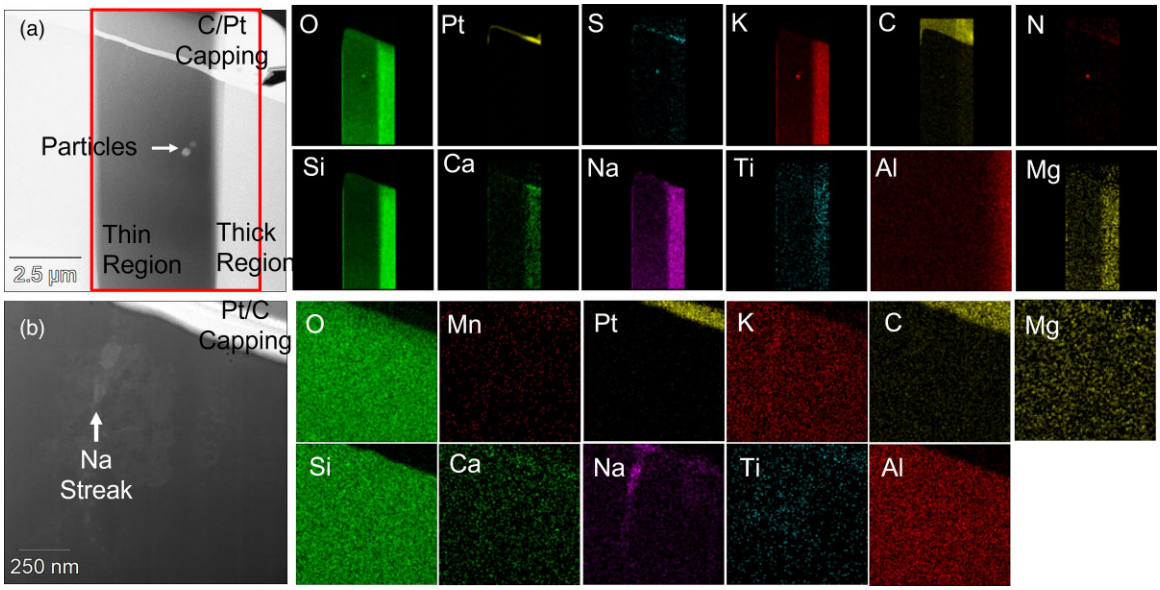

Fig. 3. STEM-HAADF images showing (**a**) a thinned window (thicker part has more counts due to more material) in the mostly uniform Sample 40, felsic glass from the wall interior, with net count EDS maps of the area including the little the inclusions and (**b**) an Na streak from the surface below the Pt and C capping layers and net count EDS maps of the elements.

agreement with the μ-XRD. SAED of the S-containing particle was consistent with potassium sulfate (K_2SO_4) (Supplementary Figs. 4b–4d) (Ojima et al., 1995). K_2SO_4 has been found to be present in a variety of wood ashes (Misra et al., 1993; Karkanas, 2021), so it is possible a particle from the ash was embedded in the glass during melting. As these features were not present at the glass surface, it is unlikely that they were formed through alteration. Chemical alteration of the felsic glass is localized to the surface, with a thin layer (100–150 nm) enriched in Na, Mg, and Fe (Supplementary Fig. 5b). A few streaks rich in Na within a micrometer of the surface (Fig. 3b) and a small Ca-rich region embedded at the surface (Supplementary Fig. 5a) were found. As shown by the overlay of Na and Pt in Figure 3b, the Na-enriched feature was exposed at the glass surface, therefore had the potential to be formed through alteration.

Felsic Glass from the Top Surface of the Wall in Contact with Topsoil

Felsic glass regions that were in contact with the topsoil (Sample 11, Fig. 1e), were similar to those from the wall interior. These shiny, relatively smooth but pitted regions were surrounded by rougher, dendritic regions, possible representative of quench crystallization expressed at the surface. The large swathes of relatively smooth but pitted regions contained many cracks and small patches of rough material (Fig. 4). Higher magnification images of the edges of the rough area show additional textures, including more extensive pitting, scale-like features, and dendrite-like growth (Figs. 4c, 4e, 4f). The pitting occurred as a gradient, with the largest amount near the rough area.

Further from the rough areas, the surface was smoother, and a FIB cross-section was extracted (Fig. 5a) to examine features below the surface. STEM bright field (BF) and high-angle annular dark-field (HAADF) imaging of the cross-section (Fig. 5b) showed that the felsic glass was uniform with few features, even at the surface. The only observable features were identified as small inclusions of sodium chloride (NaCl) near the surface and extending to a few μm below the surface (Figs. 5c, 5d; full net counts maps in Supplementary Fig. 6). NaCl aerosols have the potential to accelerate glass alteration by inducing the loss of the surface hydrogen bonds and the opening of the network (Palomar et al., 2017). However, the cross-section (Fig. 5c) showed very little evidence for alteration at the surface, with the only difference in chemistry being a thin (<100 nm) Na-containing layer, similar to the felsic glass from the wall interior. The cracks on the surface of the felsic glass offer the potential to accumulate water. Therefore, to examine how prolonged exposure to water might alter the glass, a region in the vicinity of a crack was extracted. The crack was filled with porous particles, some of which were Si-rich, suggesting degradation of the amorphous silica network under aqueous conditions (Supplementary Fig. 7).

Mafic Glass from the Melted Wall Interior

XCT was used to examine the three-dimensional microstructure of mafic glass that had flowed down inside the wall interior to form a drip (Sample 39). Cross-sections of the reconstruction are shown in Supplementary Figure 8. The once molten material shows high X-ray absorption contrast with respect to the material it is attached to. This contrast is most likely due to Fe enrichment in the mafic glass, which was formed from Fe-rich amphibolite, (Table 1) relative to the granitic rock to which it is attached. The lower part of the drip is uniform with only a few vesicles and fragments of entrained less-dense material (darker than the surrounding matrix). Towards the top of the drip, the sample becomes

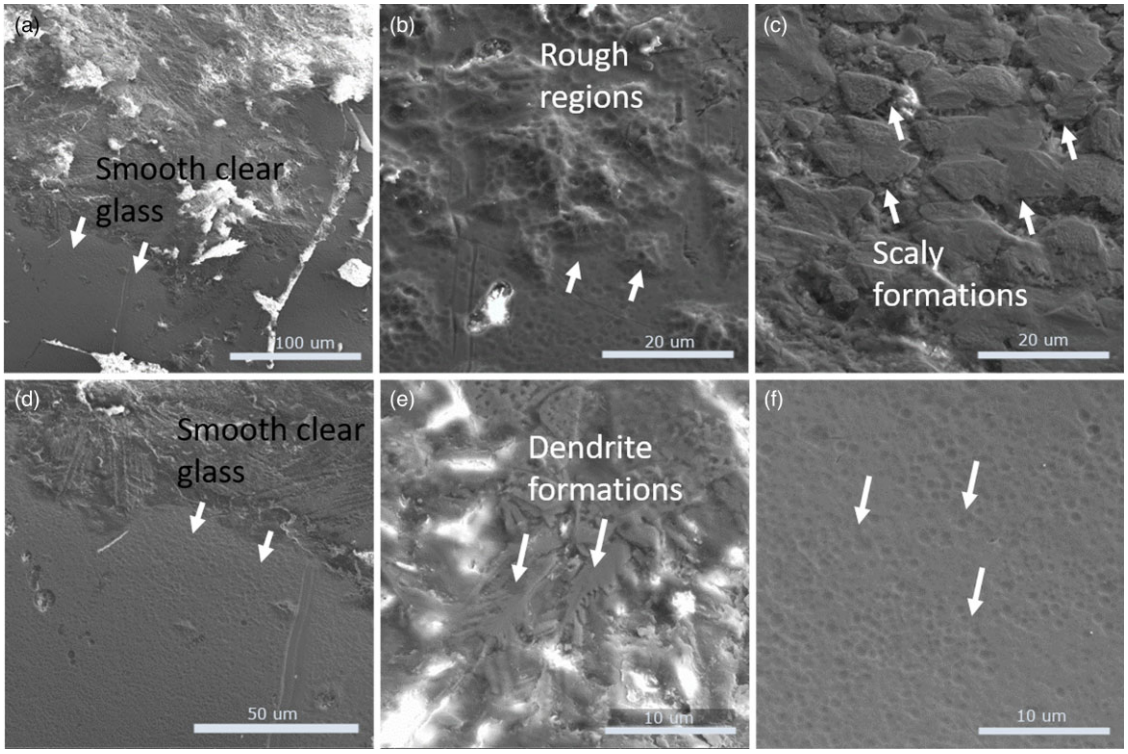

Fig. 4. SEM images of the surface of Sample 11, felsic glass from the topsoil, showing the pitted regions near by rough regions (**a**,**d**) and some of the features at the edge of the smooth glass (**b**,**c**,**e**) with arrows showing pitting in (**f**).

less X-ray absorbing/dense near the region of attachment suggesting more Fe-rich material at the base. There were many bubbles in the upper part of the drip, some of them quite large (~1 mm diameter).

The surface of the lower part of the mafic glass drip was first examined optically to identify the regions of mafic glass. The surface topography was then characterized by SEM (Fig. 6). The sample surface was textured, with varying degrees of roughness (Figs. 6a–6c). The roughness was characterized by elevated linear features (Fig. 6d), periodic ridges (Fig. 6e), and dendrites (Fig. 6f) surrounded by smoother regions all likely related to rapid crystallization of the melt during cooling after the vitrification event. Given the similar scale of the features in Figures 6e and 6f, it is possible they are different orientations of the same type of dendritic feature.

EDS maps of select regions are shown in Figure 7. Some regions had large cracks which were filled with silicon (Si)-rich material (Fig. 7a). Other regions appeared to show delamination of a flat and smooth layer at the glass surface, exposing a relatively flat surface with pitting and channeling beneath (Fig. 7b). The channels (Fig. 7b) had a higher aluminum (Al) content than the surrounding material, suggesting that the formation mechanism was driven by chemistry, but the pits were not chemically different from the matrix, suggesting a physical formation mechanism. The exposed region beneath the delaminated layer was Si poor and relatively rich in Fe (Fig. 7b). The crystalline periodic ridged regions (Fig. 7a) were relatively Si poor compared to the rougher surficial material. Other regions (Supplementary Fig. 9) were covered in C-rich material, likely organic matter, which prevented the characterization of the glass underneath.

Cross-sections of mafic glass not in contact with soil were extracted for further examination by STEM and EDS analysis (Fig. 8; full net counts EDS maps in Supplementary Fig. 10). The cross-sections were heterogeneous, with two main glassy phases: (i) a mafic Fe-, Mg-, and Ca-rich phase and (ii) a felsic Al-, K-, and Na-rich phase. These two phases intertwined in a variety of microstructural morphologies. Small (≈150 nm in diameter) nickel (Ni)-and chromium (Cr)-containing inclusions were observed (Supplementary Fig. 11). The phosphorous (P)- and Ca-rich phase in Figure 8c could be Ca phosphate, as apatite is present in the Broborg protolith and there is evidence it survives the vitrification event as rounded grains that have been partly resorbed (Vicenzi et al., 2022).

The region extracted in Figure 8a was uniform at the surface, apart from some dendritic features (like those in Fig. 6f) which likely formed during crystallization as the vitrified material cooled from the molten state. However, there were multiple crystalline and amorphous phases below the

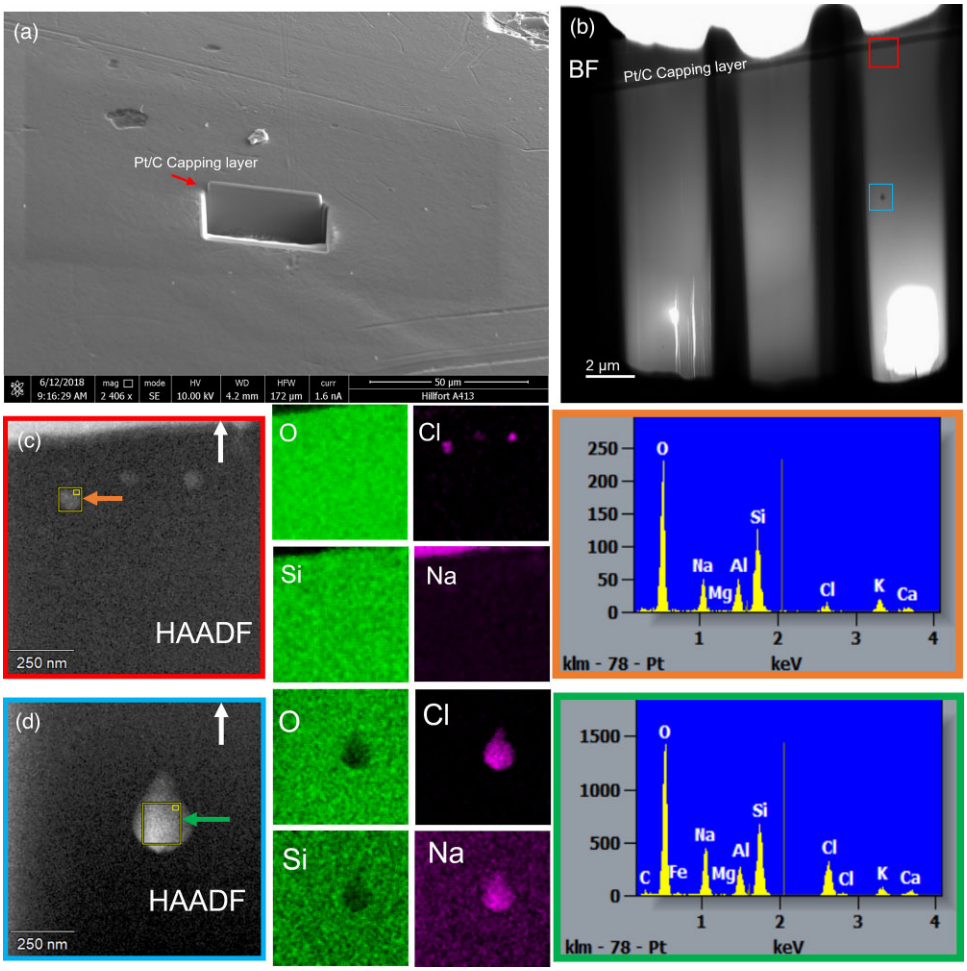

Fig. 5. SEM image (**a**) of an area extracted from Sample 11, felsic glass exposed to topsoil. BF STEM image (**b**) of the cross-section showing a smooth sample. STEM images and atomic% EDS maps with EDS spectra of inclusions near the surface (**c**) and towards the middle of the lift-out (**d**). The direction of the sample surface is indicated by the white arrows in (**c**) and (**d**).

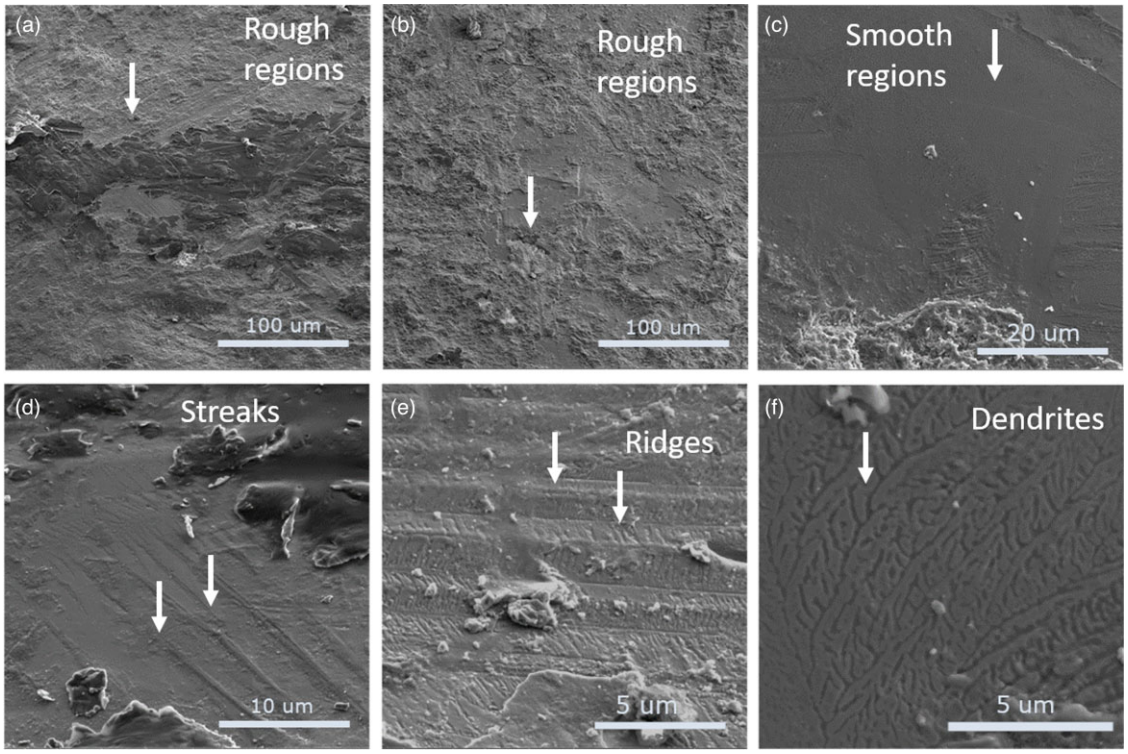

Fig. 6. SEM images showing the surface of Sample 39, mafic glass not in contact with soil, where it is rough (**a**,**b**) with streaks (**d**), ridges (**e**), and dendrite-like features (**c**,**f**).

thin surface layer of mafic glass. Si and oxygen (O) contents were similar in both phases, but the mafic glass phase contained more Mg, Fe, Ca, K, and titanium (Ti). Cross-sections of other regions showed similar layering between the two phases. Ca-containing spherical features were present in the Fe-poor phase and Ni–Cr and P-rich inclusions form in the regions between the two main phases. There was no chemical or physical variation at the surface

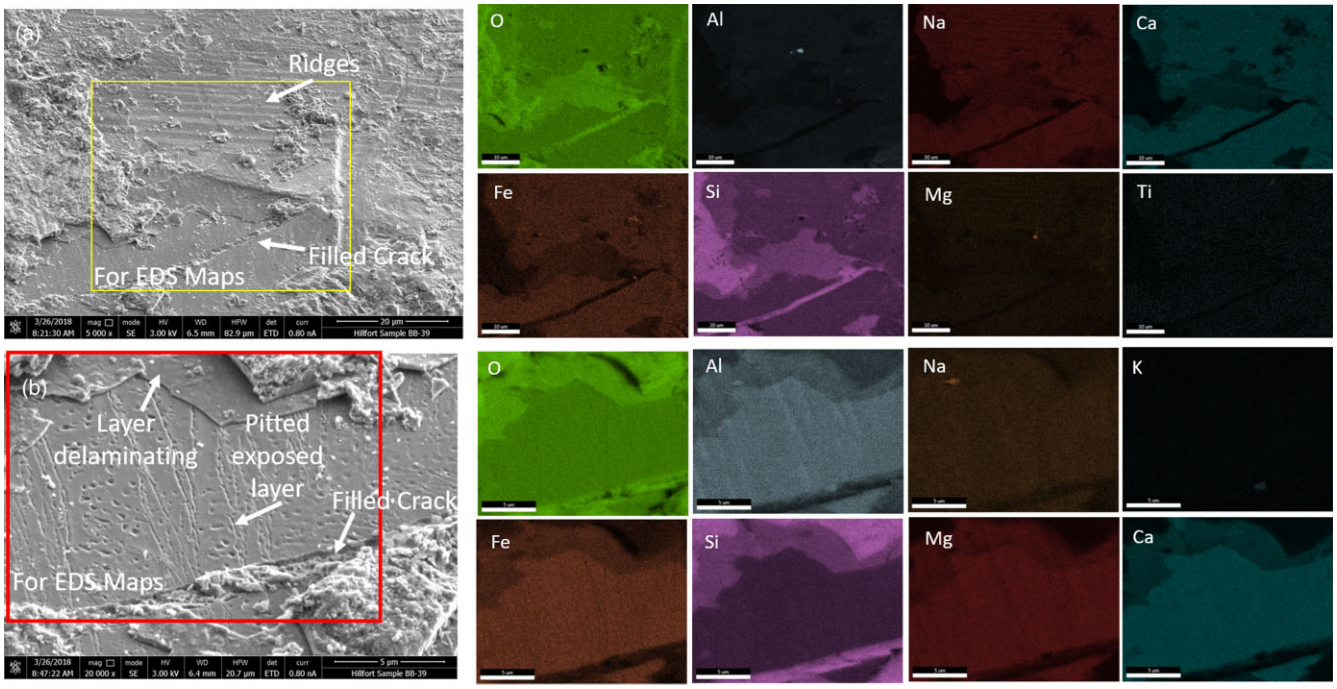

Fig. 7. SEM images (left) of the surface of Sample 39, mafic glass not in contact with soil, showing the generally rough surface with a filled crack (**a**) and a region where portions have delaminated (**b**) and corresponding net counts EDS maps (right). The scale bars for the EDS maps were 10 μm for (**a**) and 5 μm for (**b**).

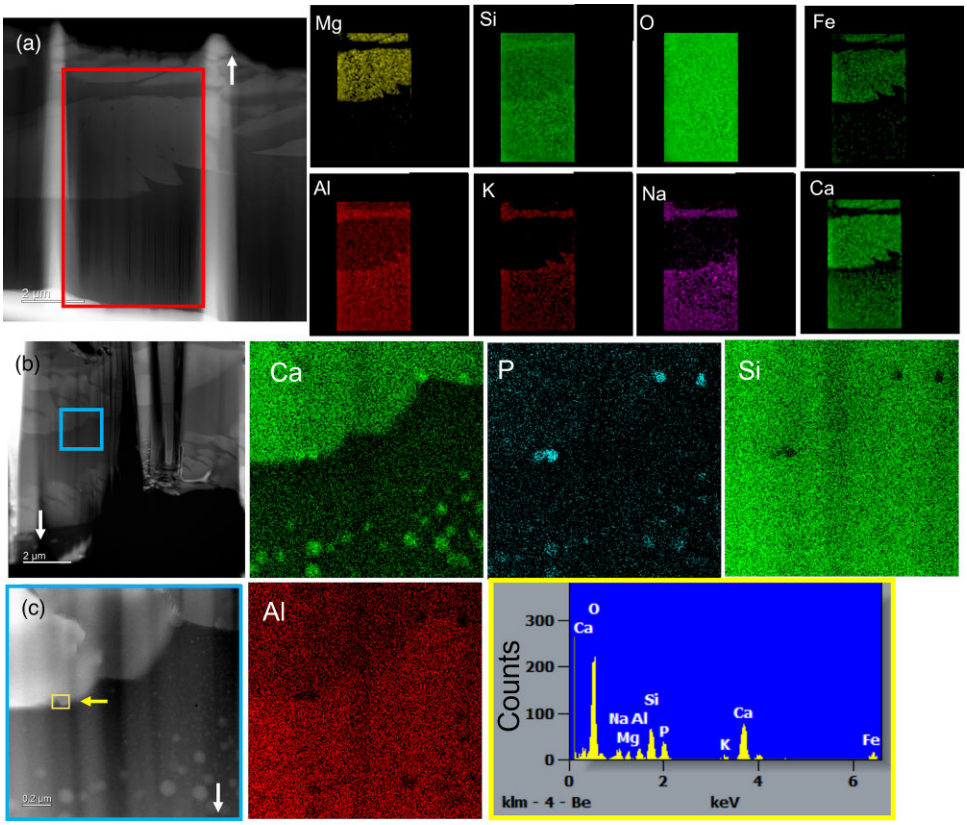

Fig. 8. STEM images of two areas (**a**,**b**) extracted from Sample 39. (**a**) shows the lamella for the top set of atomic% EDS maps (scale bar is 2 μm). (**c**) corresponds the box in (**b**) and to the images for the bottom set of atomic% EDS maps of higher concentration elements with the EDS spectrum selected for on of the P-rich areas in (**c**) (scale bar is 0.2 μm). The direction of the sample surface is indicated by the white arrows in (**a**,**b**), and (**c**).

of the glass that would suggest an alteration layer in the smooth regions selected for cross-sectional examination.

Mafic Glass from the Top Surface of the Wall in Contact with Topsoil

Optical examination of mafic glass in contact with topsoil (Sample 49b), revealed a much rougher surface (on a micron to millimeter scale) than the mafic glass extracted from the wall interior (Sample 39). This was confirmed by SEM imaging (Fig. 9 and Supplementary Fig. 12). Figures 9a–9c shows the mafic glass in contact with topsoil was covered with particles and C-rich features. The C-rich areas of the surface showed morphologies representative of fungal hyphae and the remnants of testate amoeba assemblages (Figs. 9d–9f). Other surface features, such as cracks and periodic crystalline phases (not shown), were similar to those on mafic glass from the wall interior.

A relatively flat region with a surficial crack was selected for cross-sectional analysis (Fig. 10; full maps with net counts in Supplementary Fig. 13). Due to high porosity, particularly around the crack region, the samples did not thin evenly, resulting in curtaining and over-thinning of some regions. The extracted crack region was filled with electron beam-assisted Pt and C to help protect the region during thinning. Despite these artifacts from the FIB, several alteration features were observed. The glass was highly porous beneath C-rich areas on the surface that could represent evidence of microbial colonization or other forms of alteration (Fig. 10d). This region had a partially delaminated layer that was enriched in Si. EDS line scans of the region (not shown) indicated the space below the layer is rich in C, particularly in a deeper pit in the lower surface where there was also a small, concentrated region of Na. Given that this region was localized to an area of ≈1 μm, and was below a layer of glassy material, it was hypothesized that these features are not related to C-rich material in the general topsoil and may be due to microbial activity. In addition to the delamination, a region of porous glass ran ≈0.3 μm below the surface. This porosity ran the length of the cross-section but extended deeper below the surface (1 μm) and porosity was greater near the crack. Fe was enriched at the edge of the crack, and Fe-rich material formed a bridge across the crack. A central circular feature was embedded in the side wall of the crack (Fig. 10b), with higher concentrations of O, Na, and K than the surrounding glass. Small inclusions, mostly circular, were also present as Fe–S and Ca- and Na-rich regions (Supplementary Fig. 14). Additionally, Ga lined the edge of the crack between the glass and the C deposited by the electron beam to protect the region during milling. This artifact was present because a Ga source was used for the FIB process, and Ga is deposited in crevices and cracks due to back-sputter. Typically, this artifact would be removed during low kV milling but given the fragile nature of this sample, minimal milling was used and not all of the Ga was removed.

A cross-section of mafic glass in contact with soil (Sample 49b) was extracted from the relatively flat region (Supplementary Fig. 15). The surface of the sample was rough and porous, with porosity extending to a depth of 1 μm. There were many nanosized cracks running below the surface, some of which were filled with C and Fe-rich material (not shown). There were also small bubbles, or voids, often found in the

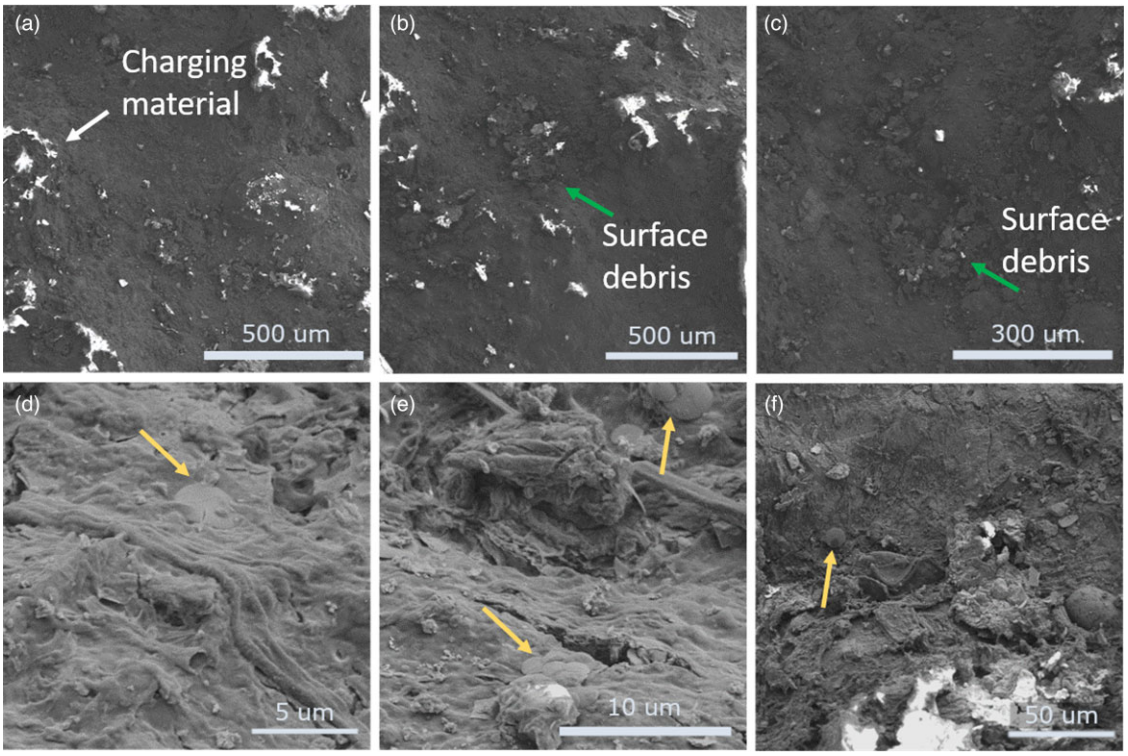

Fig. 9. SEM images of particles and debris coating the surface of Sample 49b, mafic glass in contact with soil (**a**–**c**). Note: light, white areas are areas C-rich. The morphology of the C-rich areas resembled fungal hyphae (**d**) with circular plates, highlighted with yellow arrows (arrows in bottom row) (**e**) and at lower magnification in (**f**), resulting from the breakdown of testate amoebae assemblages.

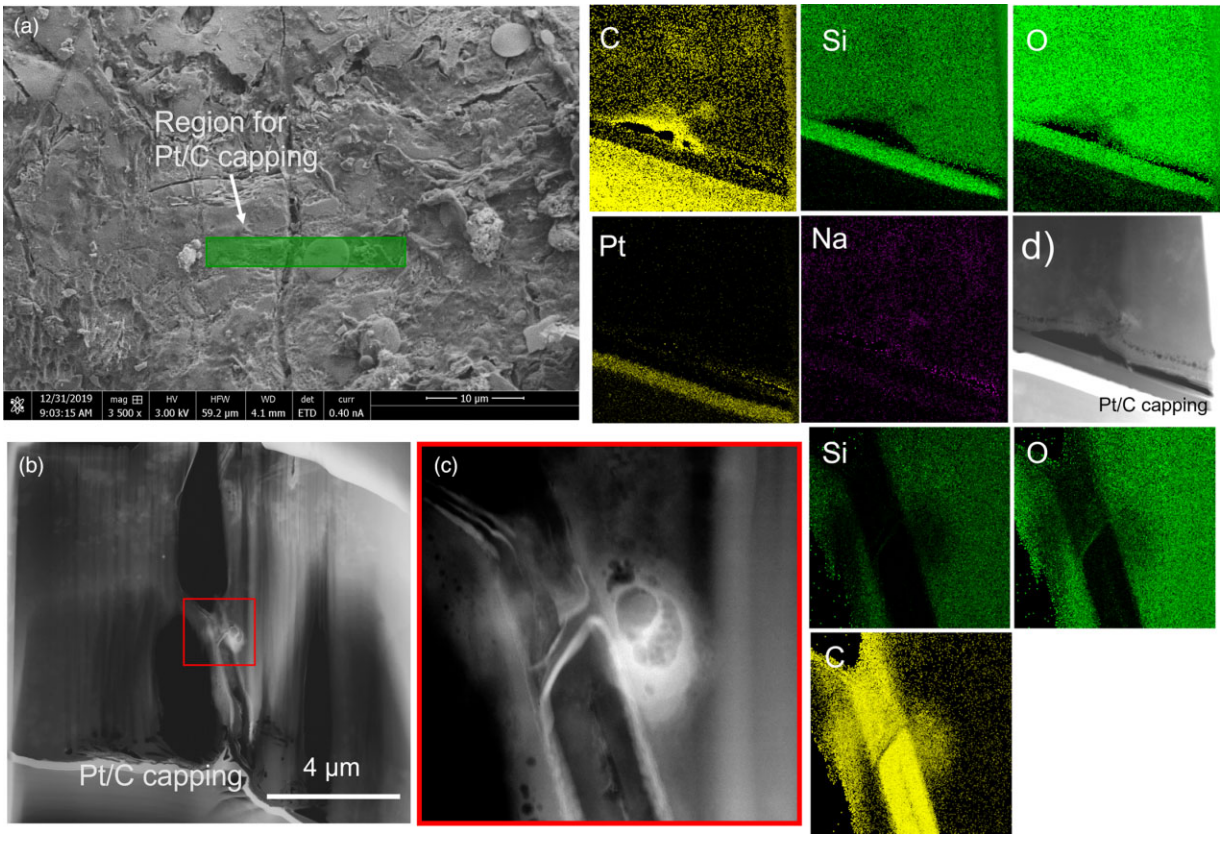

Fig. 10. SEM image of (**a**) the surface of mafic glass in contact with soil (Sample 49b), where a lamella was extracted in a crack region for STEM. (**b**) STEM-HAADF (30 kV accelerating voltage, this image only) image of the thinned lamella extracted from the green region in (**a**). (**c**) HAADF image of box in (**b**), with associated atomic% EDS maps showing the higher concentration elements. (**d**) HAADF image of glass surface with Pt and C protective coatings, with associated atomic% EDS maps of higher concentration elements.

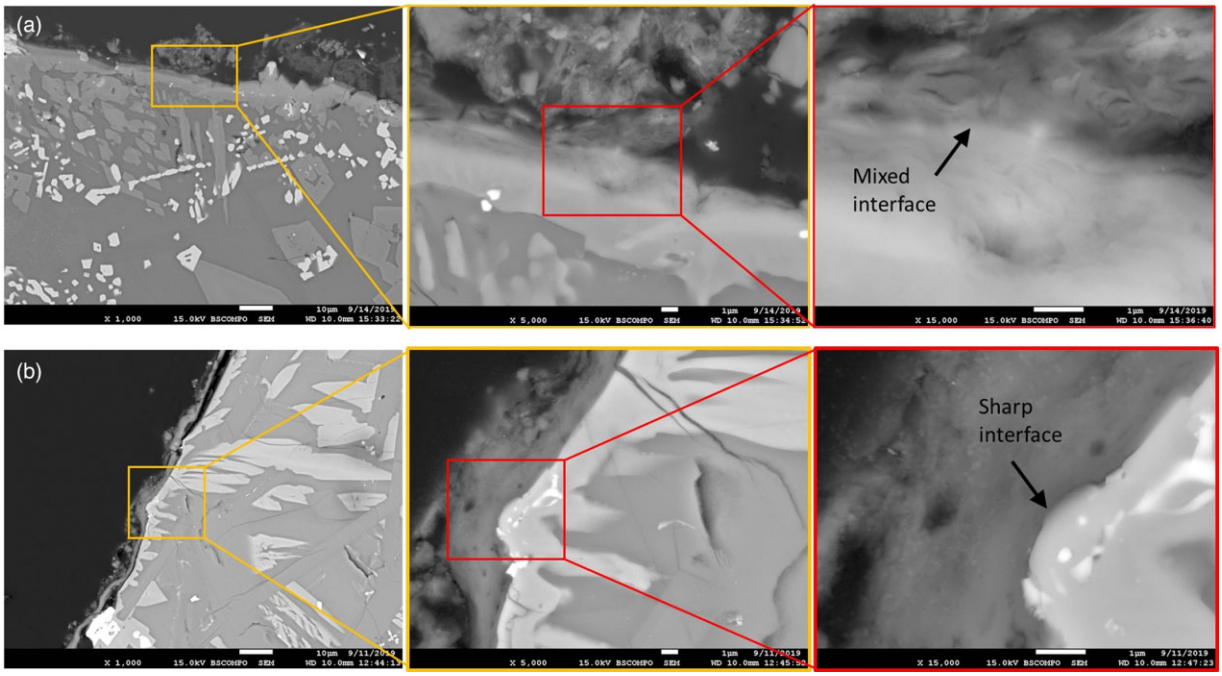

Fig. 11. Excavated Sample 49 with SEM of (**a**) the surface in contact with soil and (**b**) the surface not in contact with soil. Scale bars are 10 μm for the left-hand images and 1 μm for the center and right-hand images.

shape of rings, which located around 5 μm below the surface (Supplementary Figs. 15b–15e). Given the depth of the rings below the surface, it is possible that they represent cross-sections of bubbles that were formed during the melting and cooling of the mafic glass. More bubbles are likely to exist deeper beneath the surface, but regions extracted with the FIB-SEM only extend 10–20 μm below the surface.

Additional Nanoscale Characterization of the Surficial Layer on Mafic Glass

The surficial analysis in the section "Surficial Examination of Felsic and Mafic Glass Samples" revealed minimal alteration on the felsic glass surface, so subsequent surface characterization was only conducted on mafic glass. A sample of mafic glass that extended from the top surface of the wall into the wall interior (Sample 49, Supplementary Fig. 1c) was excavated as described

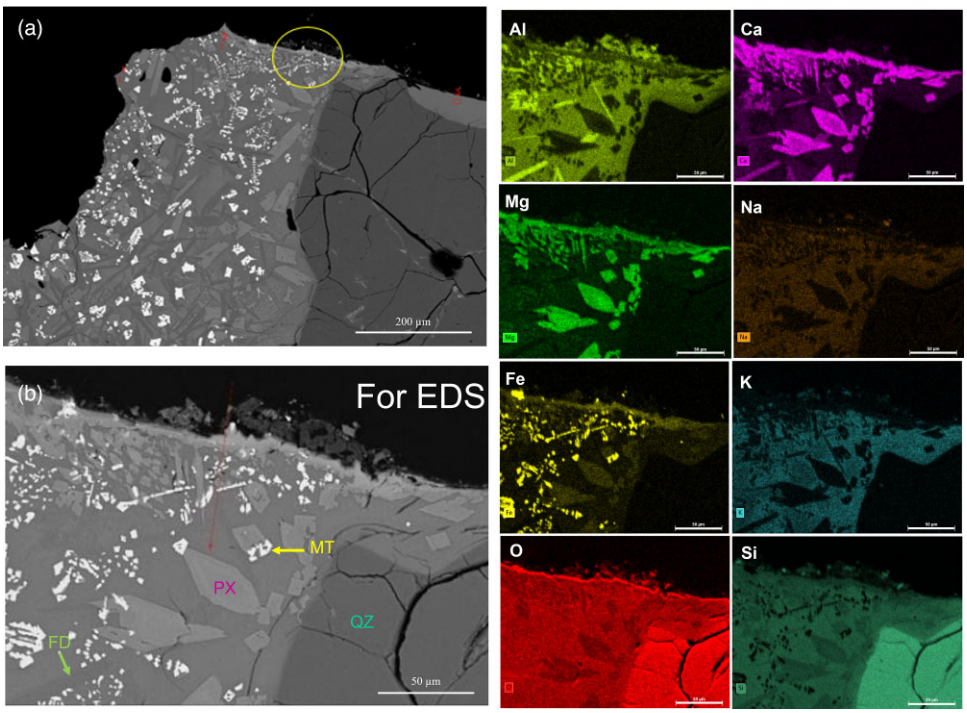

Fig. 12. Excavated Sample 49 with SEM (**a** and **b**) and EDS (**c**) of the surface in contact with soil (scale bar for EDS maps is 50 μm). Image (**b**) is a magnification of the area in the circle in image (**a**). PX, pyroxene; FD, feldspar; MT, magnetite; QZ, quartz.

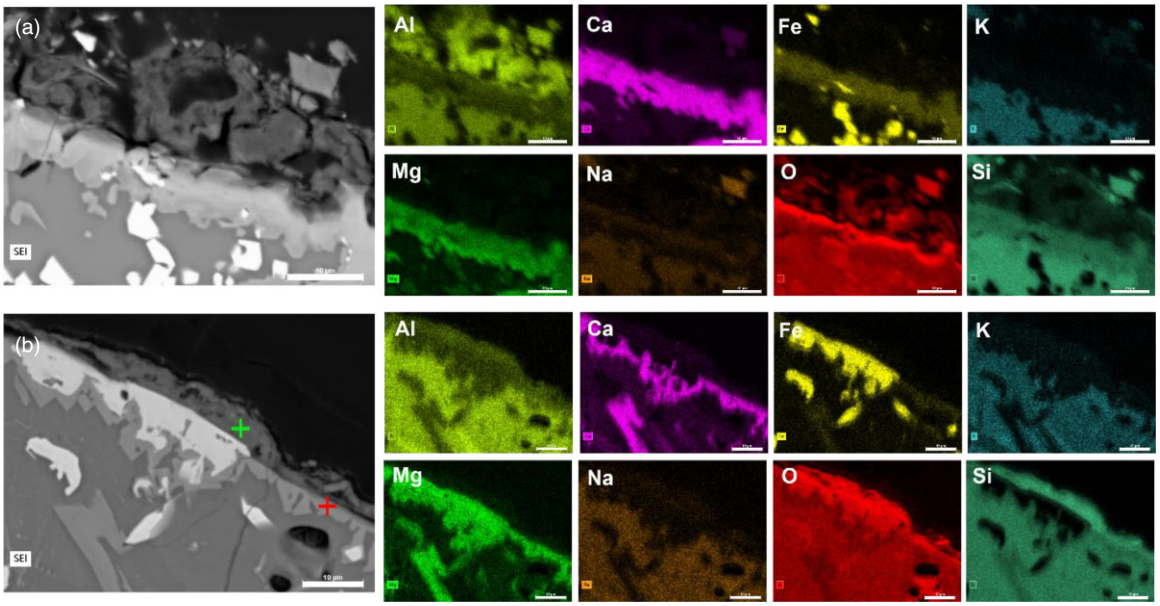

Oxide	Wt% from EDS	
	Surface glass	Mafic glass
Fe_2O_3	5.15%	19.78%
Na_2O	0.48%	0.72%
MgO	1.31%	7.06%
Al_2O_3	5.89%	8.44%
SiO_2	79.53%	37.74%
K_2O	0.85%	0.82%
CaO	5.94%	23.15%
TiO_2	0.29%	2.3%
Total	100%	100%

Fig. 13. Excavated Sample 49 with SEM of the surface (**a**) in contact with soil and (**b**) not in contact with soil and associated EDS (scale bar for EDS maps is 10 μm). The table showing the wt% of oxides measured by EDS in the surface melt (green or left cross) and the mafic glass (red or right cross).

in the methods. Polished cross-sections were extracted from the region that had been in contact with topsoil and from the region that had been in the wall interior. The samples were analyzed by SEM and EDS (Fig. 11) to understand the thickness, morphology, and compositional variation of the surficial layer in the presence and absence of contact with topsoil. The surface of mafic glass in contact with soil is shown in Figure 11a, and the surface of mafic glass without soil contact is shown in Figure 11b. Backscattered electron images in Figure 11 show a higher average atomic number (Z) region close to the surface of the sample, corresponding to enrichment principally in Fe and Ca, with a discontinuous, thin outer layer of lower Z, enriched in Al and Si at the soil interface (Figs. 12 and 13 and Supplementary Fig. 16). This surficial layer is interpreted to be a thin melt film formed during a secondary amphibolite melt event during which the molten mafic glass, which is two orders of magnitude less viscous than the felsic glass (Vicenzi et al., 2022), flowed over the previously melted mafic and felsic material to cover all available surfaces in a thin melt film (see Fig. 1f). The thin melt film can also be seen in Figure 7b as a surficial layer with differing chemistry to the bulk mafic glass beneath.

The thickness of the melt film was measured from SEM images of cross-sections perpendicular to the mafic glass surface at six locations in the sample with soil contact and three locations in the sample without soil contact. At each measurement location, an average was calculated by taking the mean of the minimum and maximum depths and three randomly selected areas (Supplementary Table 1). Thicker regions of the melt film exhibited greater surface roughness in comparison with the thinner regions. The thickness of the melt film was in the range of 0.5–80 μm, where regions in contact with the topsoil (max thickness 80.7 μm) were generally two times thicker than the max thickness of regions not in contact with the topsoil (max thickness 10.7 μm). Given the coating is interpreted to have formed as a result of the glass melting process, rather than as a result of glass alteration, the difference in thickness of the melt film on the mafic glass in contact with topsoil may be due to factors other than the nature of the contacting environment, e.g., the surface tension and flow rate of the melt film.

SEM images show the heterogeneity of the mafic glass, with pyroxene, spinel, feldspar, and quartz crystals (as identified by XRD) within the glassy matrix (Figs. 12 and 13). Higher magnification images of the melt film at the surface of the mafic glass reveal different textures at the film and mafic glass interface in the two sample types (with soil contact and without soil contact). A thicker, more fibrous film region and a less defined interface appears on the surface in contact with soil, and a thinner layer containing particulates with a sharp interface develops on the surface not in contact with soil (Fig. 11). Corresponding higher magnification SEM-EDS (Fig. 13)

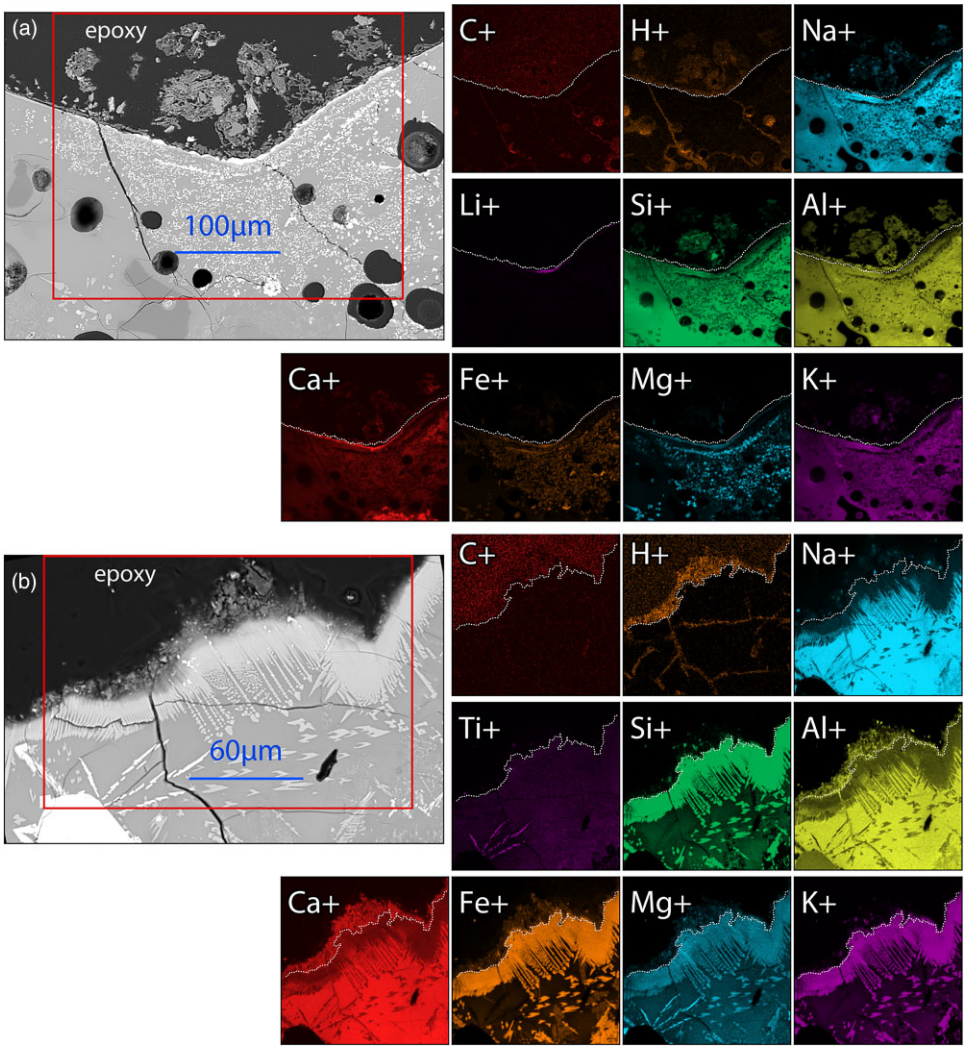

Fig. 14. Excavated mafic glass (Sample 49) with SEM (**a** and **b**) and corresponding positive ion ToF-SIMS of the surface in contact with soil (**a**) and not in contact with soil (**b**). The large C-rich regions correspond to the epoxy the sample was mounted in. A thin dotted line has been added to show the boundary between the hydrated region and the mafic glass film.

confirms that the melt film on the surface is rich in Al and Si, and that the surface in contact with the melt film consists of a continuous layer of a phase rich in Ca, Fe, and Mg. The table in Figure 13 shows the comparative wt% of oxides measured by EDS in the mafic glass and surface melt in regions similar to that shown in Figure 13b. To determine if the surficial layer was hydrated, the samples in contact with soil and not in contact with soil were analyzed by ToF-SIMS. Positive secondary ion maps (Fig. 14) show the mafic glass film and the surface layer. The map showing H indicates the cracks in the glass and the surface is hydrated and is strongly associated with the Al map above the mafic glass (boundary of H shown by the white dotted line) in both samples. It is concluded that a thin film on the surface of the mafic glass has become hydrated, i.e., water has diffused into it. Glasses containing lower amounts of SiO_2, such as those analyzed by ToF-SIMS, are generally more susceptible to alteration than those containing higher amounts of SiO_2. However, even though these glasses have been exposed to hydraulically unsaturated conditions in the presence of soil and its associated microbiome for over 1,500 years, no chemical or physical alteration beyond hydration was observed.

EBSD analysis was used to identify the crystalline phases in the bulk and at the surface of the polished cross-sections of mafic glass in contact with soil (Sample 49, Fig. 15). Figure 15a shows the fore-scattered signal, and Figure 15b shows the pattern quality map, where the lighter (higher intensity grayscale) regions represent high-quality Kikuchi pattern detection that corresponds to crystalline regions, and the darker regions represent amorphous or nanocrystalline material. The crystalline regions that were large and consistent enough to map are shown in Figure 15c. The phases are color coded [Fig. 15c: quartz (pink), microcline feldspar (olive), titanomagnetite (red), and two clinopyroxenes, hedenbergite (bright green) and diopside (orange)]. A single scan EDS map was collected simultaneously to correlate the chemistry with the EBSD (Fig. 15d).

Diopside ($CaMgSi_2O_6$) and hedenbergite ($CaFe^2 + Si_2O_6$) form a complete solid solution series (Deer et al., 1997), therefore they have the same crystal structure and similar cell parameters. These similarities mean that EBSD phase ID cannot differentiate between these minerals based on the Kikuchi patterns alone, and additional data on the chemistry from *in-situ* EDS collected with the EBSD map must be used to determine which phase should be assigned to the pattern.

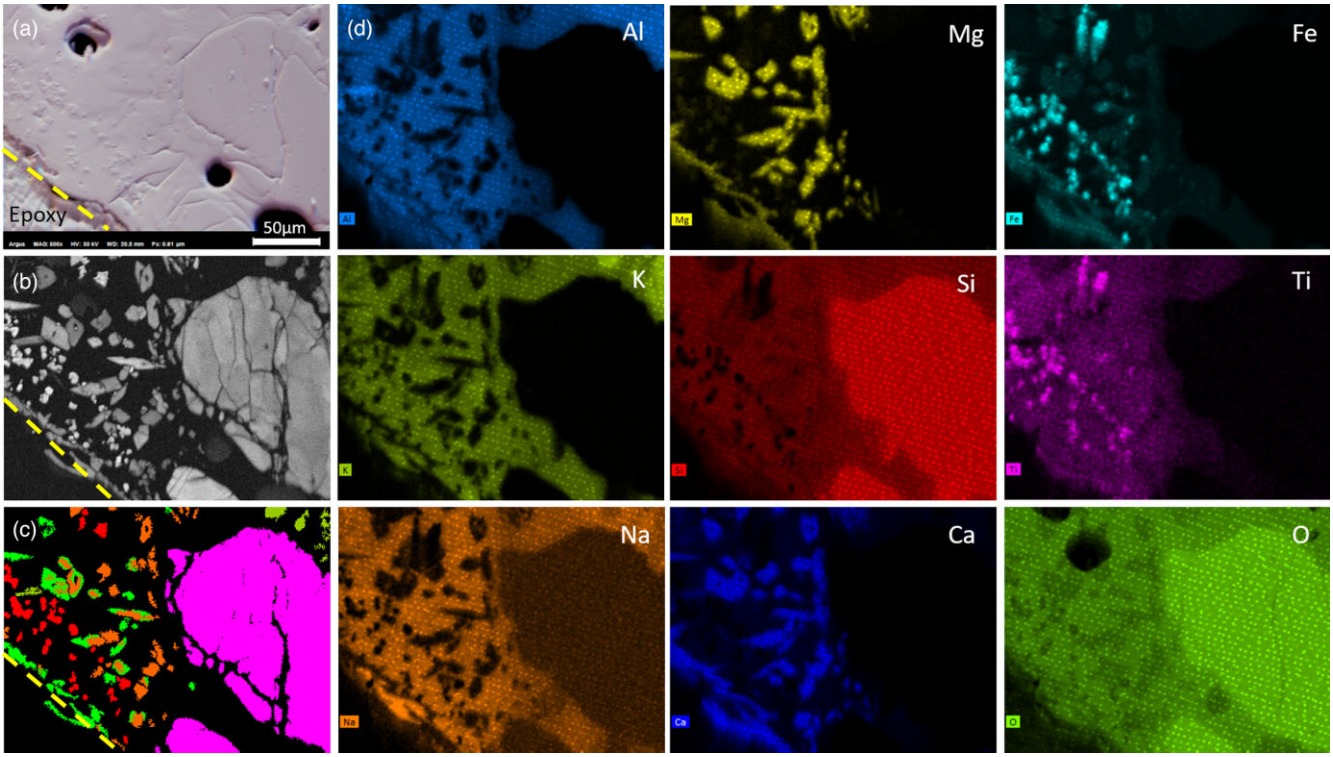

Fig. 15. (**a**) Forescatter electron image of the region on the mafic glass (Sample 49) in contact with soil analyzed By EBSD. (**b**) Forescatter image giving an indication of crystallinity. (**c**) EBSD phase map with (**d**) corresponding simultaneously collected, drift-corrected EDS maps. In (**a**,**b**), the dashed line indicates the surface of the sample with the rest of the image being epoxy. The table below gives EBSD phase information.

Some regions that have Mg signal but no signal from Fe can be assigned as diopside (orange in Fig. 15c), but the crystals assigned as hedenbergite (bright green in Fig. 15c) have EDS signal from both Mg and Fe (Fig. 15d) and likely fall on the solid solution between hedenbergite and diopside.

Higher spatial resolution EBSD mapping was conducted to explore the phases present near the surface. Pyroxene along the solid solution between hedenbergite and diopside was the most common crystalline phase at the surface (Fig. 15c), as informed by the EDS mapping (Supplementary Fig. 16).

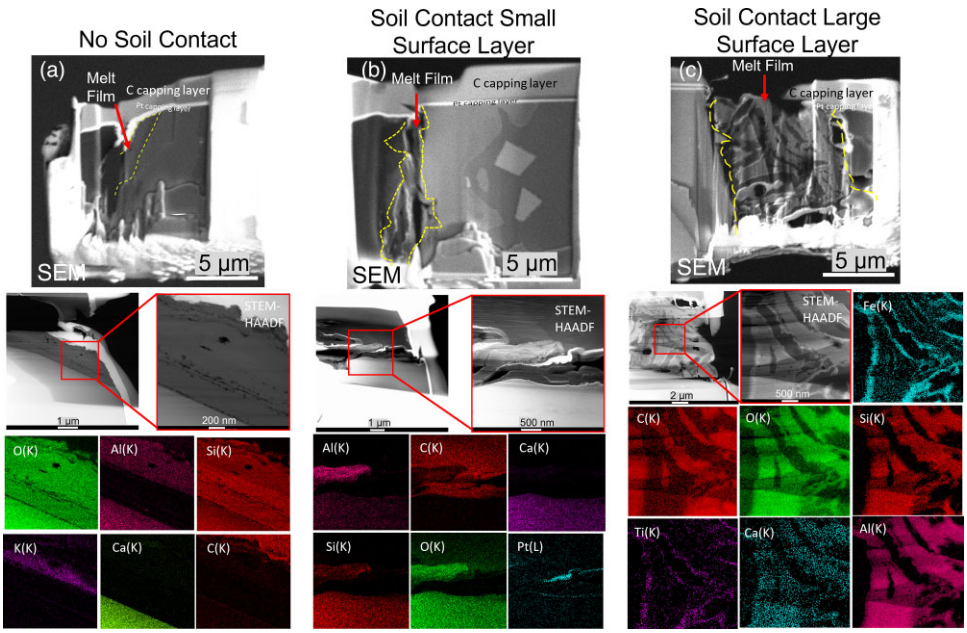

Fig. 16. Top: SEM images, middle: TEM and STEM-HAADF images, and bottom: EDS maps (rotated 90° to the SEM images) for the surface of the mafic glass (Sample 49) with no soil contact (**a**), with soil contact and a thin melt film (**b**), and with soil contact and a thick melt film (**c**). The dashed lines in the SEM images indicate the area of the sample that is the melt layer, the light gray is the melt, and the black or dark gray is the epoxy.

Pyroxene was formed during the cooling of melted amphibolite rock under oxidizing conditions (McCloy et al., 2021). The melted amphibolite is also believed to have produced the mafic glass (Weaver et al., 2018). Pyroxene is often present as either large, polygonal (euhedral) crystals in the bulk (see Figs. 11–13, 15) or as thin, nongeometric (anhedral) crystal agglomerates at the surface of the glass beneath the melt film (see Figs. 11, 14). Given the evidence that the pyroxenes formed during cooling, superficial crystallization was likely promoted by heterogeneous nucleation on the melt surface. The disparity in crystallite sizes between the large crystals in the bulk and the thinner crystals at the surface suggests that the surface cooled more rapidly than the bulk based on the relationship of cooling rate and crystal size and morphology in silicate crystals (Kirkpatrick, 1975). Equilibrium mineralogical calculations of the Broborg amphibolite predict that spinel is most stable at >1,200°C followed by feldspar and pyroxene at >1,200°C, further supported by *in-situ* high-temperature XRD (McCloy et al., 2021). It is hypothesized that the melt film was the result of a second melting event. The yellow dashed line in Figures 15a–15c indicates the suggested boundary between the glass surface and the melt film. The melt film is dark in Figure 15a, suggesting that it is amorphous or nanocrystalline. Spot analysis EBSD patterns in this region were not distinct and could not be definitively matched, therefore the melt film is likely amorphous rather than nanocrystalline (Supplementary Fig. 17). This outermost, amorphous melt film that surrounds and overlays the pyroxene consists of Si and Al and is enriched in alkali (Na and K).

Three FIB cross-sections of the melt film on the mafic glass (Sample 49), both in contact and not in contact with topsoil, were extracted from the larger polished cross-section for TEM analysis (Fig. 16). SAED in HRTEM mode was performed to determine if the melt film was completely amorphous, as suggested by EBSD, or if nanoscale regions of crystallinity, beyond the resolution of EBSD, were present. No nanocrystalline phases were observed and the melt film was completely amorphous in the three sections analyzed.

Analysis of the cross-section that was not in contact with topsoil revealed a thin micrometer-scale melt film on top of the pyroxene crystal at the surface of the mafic glass (Fig. 16a). The melt film was formed of two layers with distinct chemistry: (i) a layer adjacent to the pyroxene that was rich in SiO_2 but depleted in Al and K and (ii) an outer layer that was depleted in Si but enriched in Al and K with some Fe and Ca. The thin melt film on top of a pyroxene crystal at the surface of the mafic glass in contact with soil (Fig. 16b) was significantly enriched in Al and depleted in Si, with some Fe and Ca. The thicker (~10 μm) melt film on top of the pyroxene crystal at the surface of the mafic glass in contact with top soil (Fig. 16c) consisted of an amorphous phase with a "ribbon-like" structure that was highly porous and rich in Si, Al, and Ca, with a rind on the "ribbons" that was rich in Fe and titanium (Ti). These amorphous ribbons were surrounded by C-rich areas which are chemically consistent with the surrounding epoxy. The analysis of these three cross-sections highlights the variability in texture and chemistry of the melt film and demonstrates that the differences do not seem to be related to the nature of the environment with which the film was in contact and are likely due to factors related to the melt conditions, e.g., surface tension and the flow rate of the melt film.

The composition of the mafic glass is comparable to basaltic volcanic glass with a relatively low silica content. The alteration of volcanic glass, including the formation of secondary products, has been studied extensively (Stroncik & Schmincke, 2002; Hausrath et al., 2008; Cockell et al., 2009), as it can have a significant impact on the chemistry of natural waters (Stumm & Morgan, 1996). Because of their thermodynamic instability, glasses can be more reactive than mineral assemblages, and alteration is the consequence of the interaction of glass with aqueous solutions. It is generally accepted that palagonite, a heterogeneous material with highly variable structural properties, is the first stable product of mafic glass alteration in contact with water, on a timescale of tens of thousands of years (Stroncik & Schmincke, 2002). The abundance of alteration features is controlled by the chemistry of the glass, with silica-rich glass, e.g., obsidian, weathering more slowly than less silica-rich materials such as basaltic glass (Thorseth et al., 1991). The chemistry and crystallinity of the melt films in Figure 16 are dissimilar to those observed for the glass-palagonite transformation at various stages and on glasses of varied compositions (Furnes, 1975; Thorseth et al., 1991). Palagonite is a heterogeneous substance composed of crystalline clays, zeolites, and oxides, whereas the melt film is completely amorphous. The formation of the purely amorphous "gel-palagonite" has been documented, but this is related to Si, Al, Mg, Ca, Na, and K loss, H_2O gain, and immobile Ti and Fe behavior, whereas the melt films in Figure 16 are enriched in Al, K, Fe, and Ca (Stroncik & Schmincke, 2002). It is concluded that the thin melt film on the surface of the mafic glass has been hydrated, i.e., water has diffused into it, but no other chemical or physical alteration has occurred, even though it is relatively low in SiO_2 in some cases, and after exposure to hydraulically unsaturated conditions in the presence of soil and its associated microbiome for over 1,500 years.

Discussion of Surficial Features

Analysis of these archeological glass samples excavated from Broborg, a Swedish hillfort dating from 400 to 550 CE, provides a unique opportunity to understand how glass chemistry influences the interaction of glass with the environment over prolonged time periods. The mafic and felsic glasses examined had different surficial textures and chemistries. The chemistry of the felsic, high SiO_2 glass was uniform, consisting of one phase with some salt inclusions. The felsic glass showed limited chemical alteration, consistent with Si-rich glasses being more resistant to alteration (Furnes, 1975; Vienna & Crum, 2018), with a thin layer (<150 nm) enriched in Na for samples both in contact with topsoil and within the wall interior. Na enrichment at the surface is the opposite of what would be expected for the alteration of alkali-silicate glasses in an aqueous solution. The initial phase of alteration usually involves the replacement of alkali ions in the glass by a hydronium (H_3O^+) ion from the solution, resulting in alkali depletion of the near surface (Doremus, 1975; McGrail et al., 2001; Ojovan et al., 2006). However, dominant alteration mechanisms are different in unsaturated conditions (Ojovan et al., 2005), and repeated wetting of the surface could result in Na leaching and subsequent accumulation during the groundwater drying process. The felsic glass surface did show some physical alteration in the form of pitting, which is considered a possible signature of alteration by either abiotic or biotic processes (Weaver et al., 2021). However, no evidence for microbial colonization was found on the surface of the felsic glass.

Examination of cracks in the felsic glass where water could be retained for longer periods than on the surface showed an alteration of a few micrometers.

The mafic, low SiO_2 glass was heterogeneous and had pyroxene, spinel, feldspar, and quartz crystals within the glassy matrix. The mafic glass surfaces in contact with topsoil were rougher than those in the wall interior and, while direct observation of microbial activity was notably absent on the felsic glass, the mafic glass surface had carbon-rich material in morphologies consistent with microbial colonization (fungal hyphae, etc.). From EBSD and SAED analysis, the dominant phase at the surface of the mafic glass was pyroxene, which crystallized during the cooling of the melt produced during the heating of amphibolite rock, as determined by McCloy et al. (2021). Pyroxene would have been the major silicate mineral present in the melt at 1,200°C and may have crystallized at the surface through heterogeneous nucleation, with the other minerals, such as quartz, crystallizing at lower temperatures. On top of the pyroxene, an amorphous melt film exhibiting a variety of different thicknesses (<5–80 μm), textures and chemistries coated all exposed surfaces, and it is hypothesized that this melt film was the result of a secondary melting event. The chemistry and texture of the melt film were unlike those observed for palagonite, the first stable product of mafic glass alteration. Thus, it is concluded that the thin melt film on the surface of the mafic glass remained substantially unaltered, even though it was relatively low in SiO_2 in some cases, and after exposure to hydraulically unsaturated conditions in the presence of soil and its associated microbiome for ~1,500 years.

Conclusion

Here, the various surficial features that are formed on glass under near-surface conditions in the environment over hundreds of years have been cataloged. Alteration of the glass from Broborg did not result in the formation of phases that could be identified as crystalline, therefore comparisons could not be made with phases that are allowed to precipitate in the current IDF glass dissolution model (Freedman et al., 2015). Broborg felsic glass rich in Si, Al, and K exhibited limited alteration, with some pitting and chemical alteration features on the scale of nanometers. Broborg mafic glass rich in Fe, Mg, and Ca showed evidence of microbial colonization in the form of an organic-rich layer. Increased porosity of the glass beneath this organic-rich layer was observed up to a depth of ~1 μm, as has been seen in previous studies on the microbiologically induced deterioration of glass (Koestler et al. 1987). Despite this alteration, the thin film that was formed when the amphibolite melted, and molten mafic glass covered all available surfaces, was still present. The formation of a hydrated amorphous Al-rich layer on the surface of the mafic glass in contact with soil could indicate the initial stages of the palagonitization process, which is accompanied by the mobilization of elements, resulting in the enrichment of Al, K, Fe, and Ca in this case. If the residual rate for a collection of seventeen LAW glass alteration experiments [$(5.4 \pm 9.6) \times 10^{-4}$ g/m^2/d] is assumed (Parruzot & Crum, 2021), the average thickness of the alteration layer on these glasses would be ~108 μm after 1,500 years. Thus, the maximum alteration layer thickness of ~1 μm on the Broborg samples is up two orders of magnitude less than the thickness measured for LAW glasses subjected to laboratory testing. The limited alteration of vitrified material with aluminosilicate chemistry similar to that of LAW glass after exposure to the mostly temperate conditions at the Broborg hillfort for over 1,500 years supports the long-term durability of LAW glass disposed in the semi-arid climate of the IDF at Hanford.

Supplementary material

To view supplementary material for this article, please visit https://doi.org/10.1093/micmic/ozac032.

Acknowledgments

The authors give special thanks to Uppsala County Administrative Board for permission to conduct an archaeological field survey and to Fredrik Larsson and Torbjörn Jakobsson Holback (The Archaeologists, National Historical Museums) for conducting the excavation. We gratefully acknowledge Professor Peter Kresten for supplying the original vitrified samples from Broborg. A portion of the research was performed using the Environmental Molecular Sciences Laboratory (EMSL), a national scientific user facility sponsored by the DOE's Office of Biological and Environmental Research located at Pacific Northwest National Laboratory under proposal number 51,400.

Certain commercial products are identified in this paper to specify the experimental procedures in adequate detail. This identification does not imply recommendation or endorsement by the authors or by the National Institute of Standards and Technology or Department of Energy, nor does it imply that the products identified are necessarily the best available for the purpose. Contributions of the Department of Energy and the National Institute of Standards and Technology are not subject to copyright.

Financial support

This work is partially supported by the United States Department of Energy (US DOE) Office of Environmental Management, International Programs, and by the US DOE Waste Treatment and Immobilization Plant Project.

Conflict of interest

The authors declare no competing interests.

References

Alexander WR, Reijonen HM & McKinley IG (2015). Natural analogues: Studies of geological processes relevant to radioactive waste disposal in deep geological repositories. *Swiss J Geosci* **108**(1), 75–100.

Birkholzer J, Houseworth J & Tsang C-F (2012). Geologic disposal of high-level radioactive waste: Status, key issues, and trends. *Annu Rev Environ Resour* **37**, 79–106.

Cockell CS, Olsson-Francis K, Herrera A & Meunier A (2009). Alteration textures in terrestrial volcanic glass and the associated bacterial community. *Geobiology* **7**, 50–65.

Crovisier JL, Advocat TJ, Petit JC & Fritz B (1988). Alteration of basaltic glass in Iceland as a natural analogue for nuclear waste glasses: Geochemical modelling with DISSOL. *MRS Online Proc Lib* **127**, 57–64.

Deer WA, Howie RA, & Zussman J (1997). *Rock-Forming Minerals, Single-Chain Silicates, vol. 2A*, p. 199. London: The Geological Society.

DOE (2017). *Performance Assessment for the Integrated Disposal Facility, Hanford Site*. Richland, WA: Washington River Protection Solutions, LLC.

Doremus RH (1975). Interdiffusion of hydrogen and alkali ions in a glass surface. *J Non-Cryst Solids* **19**, 137–144.

Englund M, Heimdahl J, Larsson F, Magnell O & Ogenhall E (2018). *Broborg Hillfort: A Research Study of the Vitrified Wall*, pp. 1–60. Report Uppsala: The National Historical Museums.

Ewing RC & Roed G (1987). Natural analogues: Their application to the prediction of the long-term behavior of nuclear waste glasses. *Mater Res Soc Symp Proc* **84**, 67–83.

Freedman VL, Ryan JV & Bacon DH (2015). *Immobilized low-activity waste glass release data package for the integrated disposal facility performance assessment. Report PNNL-24615*. Richland, WA: Pacific Northwest National Laboratory.

Frugier P, Gin S, Minet Y, Chave T, Bonin B, Godon N, Lartigue JE, Jollivet P, Ayral A, De Windt L & Santarini G (2008). SON68 nuclear glass dissolution kinetics: Current state of knowledge and basis of the new GRAAL model. *J Nucl Mater* **380**, 8–21.

Frugier P, Minet Y, Rajmohan N, Godon N & Gin S (2018). Modeling glass corrosion with GRAAL. *NPJ Mater Degradat* **2**, 35.

Furnes H (1975). Experimental palagonitization of basaltic glasses of varied compositions. *Contrib Mineral Petrol* **50**, 105–113.

Goel A, McCloy JS, Pokorny R & Kruger AA (2019). Challenges with vitrification of Hanford high-level waste (HLW) to borosilicate glass – An overview. *J Non-Cryst Solids: X* **4**, 100033.

Grambow B (2006). Nuclear waste glasses – How durable? *Elements* **2**, 357–364.

Hausrath EM, Treiman AH, Vicenzi E, Bish DL, Blake D, Sarrazin P, Hoehler T, Midtkandal I, Steele A & Brantley SL (2008). Short- and long-term olivine weathering in Svalbard: Implications for Mars. *Astrobiology* **8**, 1079–1092.

Hoitink D, Burk K, Ramsdell Jr. J & Shaw WJ (2005). *Hanford site climatological summary 2004 with historical data. Report PNNL-15160. Richland*. Washington, USA: Pacific Northwest National Laboratory.

Karkanas P (2021). All about wood ash: Long term fire experiments reveal unknown aspects of the formation and preservation of ash with critical implications on the emergence and use of fire in the past. *J Archaeol Sci* **135**, 105476.

Kirkpatrick R (1975). Crystal growth from the melt: A Review. *Am Mineral* **60**, 798–814.

Koestler RJ, Santoro ED, Ransick L, Brill RH & Lynn M (1987). Preliminary scanning electron microscopy study of microbiologically induced deterioration of high alkali low-lime glass. In *Biodeterioration Research 1*, Llewlly GC & O'Rear CE (Eds.), pp. 295–307. Boston, MA: Springer.

Kresten P & Ambrosiani B (1992). Swedish vitrified forts: A reconnaissance study. *Fornvännen J Swedish Antiquarian Res* **87**, 1–17.

Kresten P, Kero L & Chyssler J (1993). Geology of the vitrified hill-fort Broborg in Uppland, Sweden. *Geologiska Föreningen i Stockholm Förhandlingar* **115**, 13–24.

Le Bas MJ, Le Maitre RW, Streckeisen A & Zanettin B (1986). A chemical classification of volcanic rocks based on the total alkali-silica diagram. *J Petrol* **27**, 745–750.

Macquet C & Thomassin JH (1992). Archaeological glasses as modelling of the behavior of buried nuclear waste glass. *Appl Clay Sci* **7**, 17–31.

McCloy JS (2019). Frontiers in natural and un-natural glasses: An interdisciplinary dialogue and review. *J Non-Cryst Solids: X* **4**, 100035.

McCloy JS, Marcial J, Clarke JS, Ahmadzadeh M, Wolff JA, Vicenzi EP, Bollinger DL, Ogenhall E, Englund M, Pearce CI, Sjöblom R & Kruger AA (2021). Reproduction of melting behavior for vitrified hillforts based on amphibolite, granite, and basalt lithologies. *Sci Rep* **11**, 1272.

McGrail BP, Bacon DH, Icenhower JP, Mann FM, Puigh RJ, Schaef HT & Mattigod SV (2001). Near-field performance assessment for a low-activity waste glass disposal system: Laboratory testing to modeling results. *J Nucl Mater* **298**, 95–111.

Michelin A, Burger E, Leroy E, Foy E, Neff D, Benzerara K, Dillmann P & Gin S (2013). Effect of iron metal and siderite on the durability of simulated archeological glassy material. *Corros Sci* **76**, 403–414.

Miller WM, Chapman N, McKinley I, Alexander R & Smellie J (1994). Introduction. In *Studies in Environmental Science*, vol. **57**, Chapter 1, Miller W, Alexander R, Chapman N, McKinley I & Smellie J (Eds.), pp. 1–22. Amsterdam: Elsevier.

Misra MK, Ragland KW & Baker AJ (1993). Wood ash composition as a function of furnace temperature. *Biomass Bioenergy* **4**, 103–116.

Murphy WM (2000). Natural analogs and performance assessment for geologic disposal of nuclear waste. *Mater Res Soc Symp Proc* **608**, 533–544.

Nava-Farias L, Neeway JJ, Schweiger MJ, Marcial J, Canfield NL, Pearce CI, Peeler DK, Vicenzi EP, Kosson DS, Delapp RC, McCloy JS, Walling SA, Thorpe CL, Corkhill CL, Hand RJ, Sjöblom R & Kruger AA (2021). Applying laboratory methods for durability assessment of vitrified material to archaeological samples. *NPJ Mater Degradat* **5**(1), 57.

Neeway JJ, Kerisit SN, Liu JJZ, Zhu Z, Riley B & Ryan JV (2016). Ion-exchange interdiffusion model with potential application to long-term nuclear waste glass performance. *J Phys Chem C* **120**, 9374–9384.

Neeway JJ, Rieke PC, Parruzot BP, Ryan JV & Matthew Asmussen R (2018). The dissolution behavior of borosilicate glasses in far-from equilibrium conditions. *Geochim Cosmochim Acta* **226**, 132–148.

Ogenhall E (2016). Amphibolitic rocks near Broborg, Uppland. Chemical and mineralogical analyses of metamorphic mafic-intermediate rocks from outcrops near the prehistoric vitrified hillfort Broborg and a Boulder in the hillfort. Report RAÄ 156:1. Sweden, Uppland, Knivsta, Husby-Långhundra. Statens historiska museer. Geoarkeologisk undersökning. Arkeologerna. Geoarkeologiskt Laboratorium. GAL PM 3.

Ojima K, Nishihata Y & Sawada A (1995). Structure of potassium sulfate at temperatures from 296 K down to 15 K. *Acta Crystallogr Sect B: Struct Sci* **51**, 287–293.

Ojovan MI, Hand RJ, Ojovan NV & Lee WE (2005). Corrosion of alkali-borosilicate waste glass K-26 in non-saturated conditions. *J Nucl Mater* **340**, 12–24.

Ojovan MI, Pankov A & Lee WE (2006). The ion exchange phase in corrosion of nuclear waste glasses. *J Nucl Mater* **358**, 57–68.

Palomar T, Chabas A, Bastidas DM, de la Fuente D & Verney-Carron A (2017). Effect of marine aerosols on the alteration of silicate glasses. *J Non-Cryst Solids* **471**, 328–337.

Parruzot B & Crum JV (2021). *FY2021 Report: ILAW glass stage II and III static dissolution testing and modeling*. Report Richland, WA, Pacific Northwest National Laboratory.

Pierce EM, McGrail BP, Rodriguez EA, Schaef HT, Saripalli P, Serne RJ, Krupka KM, Martin PF, Baum SR, Geiszler KN, Reed LR & Shaw WJ (2004). *Waste form release data package for the 2005 integrated disposal facility performance assessment. Report, Pacific Northwest National Lab. (PNNL)*, Richland, WA, USA: Medium: ED; Size: PDFN.

Pierce EM, Reed LR, Shaw WJ, McGrail BP, Icenhower JP, Windisch CF, Cordova EA & Broady J (2010). Experimental determination of the effect of the ratio of B/Al on glass dissolution along the nepheline ($NaAlSiO_4$)-malinkoite ($NaBSiO_4$) join. *Geochim Cosmochim Acta* **74**, 2634–2654.

Plymale AE, Wells JR, Pearce CI, Brislawn CJ, Graham EB, Cheeke TE, Allen JL, Fansler SJ, Arey BW, Bowden ME, Saunders DL, Danna VG, Tyrrell KJ, Weaver JL, Sjöblom R, Paul R, McCloy JS, Hjärthner-Holdar E, Englund M, Ogenhall E, Peeler DK & Kruger AA (2021). Niche partitioning of microbial communities at an ancient vitrified hillfort: Implications for vitrified radioactive waste disposal. *Geomicrobiol J* **38**, 1–21.

Rani N, Shrivastava JP & Bajpai RK (2010). Obsidian: A potential natural analogue for nuclear waste glass. *Curr Sci* **98**, 950–954.

Rieke PC, Kerisit S, Ryan JV & Neeway JJ (2018). Adaptation of the GRAAL model of glass reactivity to accommodate non-linear diffusivity. *J Nucl Mater* **512**, 79–93.

Scheetz BE, Freeborn WP, Smith DK, Anderson C, Zolensky M & White WB (1985). The role of boron in monitoring the leaching of borosilicate glass waste forms. *Mater Res Soc Symp Proc* **44**, 129–134.

Sjöblom R, Ecke H & Brännvall E (2013). On the possibility of using vitrified forts as anthropogenic analogues for assessment of long-term behaviour of vitrified waste. In *Waste Management and the Environment VI*, vol. **163**, Popov V, Itoh H & Brebbia CA (Eds.), pp. 225–236. Southampton, UK: WIT Press.

Sjöblom R, Hjärthner-Holdar E, Pearce CI, Weaver JL, Ogenhall E, McCloy JS, Marcial J, Vicenzi EP, Schweiger MJ & Kruger AA (2022). Assessment of the reason for the vitrification of a wall at a hillfort. The example of Broborg in Sweden. *J Archaeol Sci: Rep* **43**, 103459.

Sjöblom R, Weaver J, Peeler D, McCloy J, Kruger AA, Ogenhall E & Hjarthner-Holdar E (2016). Vitrified hillforts as anthropogenic analogues for nuclear waste glasses – project planning and initiation. *Int J Sustain Dev Plan* **11**, 897–906.

Stroncik NA & Schmincke H-U (2002). Palagonite – a review. *Int J Earth Sci* **91**, 680–697.

Stumm W & Morgan JJ (1996). *Aquatic Chemistry, 3rd ed*. New York: John Wiley & Sons.

Thorseth IH, Furnes H & Tumyr O (1991). A textural and chemical study of Icelandic palagonite of varied composition and its bearing on the mechanism of the glass-palagonite transformation. *Geochim Cosmochim Acta* **55**, 731–749.

Vernaz É & Bruezière J (2014). History of nuclear waste glass in France. *Proc Mater Sci* **7**, 3–9.

Verney-Carron A, Gin S, Frugier P & Libourel G (2010*b*). Long-term modeling of alteration-transport coupling: Application to a fractured Roman glass. *Geochim Cosmochim Acta* **74**, 2291–2315.

Verney-Carron A, Gin S & Libourel G (2008). A fractured roman glass block altered for 1800 years in seawater: Analogy with nuclear waste glass in a deep geological repository. *Geochim Cosmochim Acta* **72**, 5372–5385.

Verney-Carron A, Gin S & Libourel G (2010*a*). Archaeological analogs and the future of nuclear waste glass. *J Nucl Mater* **406**, 365–370.

Vicenzi EP, Lam T, Weaver JL, Herzing AA, McCloy JS, Sjöblom R & Pearce CI (2022). Major to trace element imaging and analysis of iron age glasses using stage scanning in the analytical dual beam microscope (tandem). *Heritage Sci*, in press. http://dx.doi.org/10.1186/s40494-022-00707-4

Vienna JD, Crum JV (2018). Non-linear effects of alumina concentration on product consistency test response of waste glasses. *J Nucl Mater* **511**, 396–405.

Vienna JD, Ryan JV, Gin S, Inagaki Y (2013). Current understanding and remaining challenges in modeling long-term degradation of borosilicate nuclear waste glasses. *Int J Appl Glass Sci* **4**, 283–294.

Weaver JL, DePriest PT, Plymale AE, Pearce CI, Arey B & Koestler RJ (2021). Microbial interactions with silicate glasses. *NPJ Mater Degrad* **5**, 11.

Weaver JL, McCloy JS, Ryan JV & Kruger AA (2016). Ensuring longevity: Ancient glasses help predict durability of vitrified nuclear waste. *Am Ceram Soc Bull* **95**, 18–23.

Weaver JL, Pearce CI, Sjöblom R, McCloy JS, Miller M, Varga T, Arey BW, Conroy MA, Peeler DK, Koestler RJ, DePriest PT, Vicenzi EP, Hjärthner-Holdar E, Ogenhall E & Kruger AA (2018). Pre-viking Swedish Hillfort glass: A prospective long-term alteration analogue for vitrified nuclear waste. *Int J Appl Glass Sci* **9**, 540–554.

White AF & Brantley SL (2003). The effect of time on the weathering of silicate minerals: Why do weathering rates differ in the laboratory and field? *Chem Geol* **202**, 479–506.

Zhang J, Zhang Y, Collin M, Gin S, Neeway JJ, Wang T & Zhu Z (2019). Nanoscale imaging of hydrogen and sodium in alteration layers of corroded glass using ToF-SIMS: Is an auxiliary sputtering ion beam necessary? *Surf Interface Anal* **51**, 219–225.

Zhu Z, Shutthanandan V & Engelhard M (2012). An investigation of hydrogen depth profiling using ToF-SIMS. *Surf Interface Anal* **44**, 232–237.